Pressure Wave Velocity Using High-Frame-Rate Ultrasound Imaging for Urodynamic Study

by

Nova Alam

A thesis
presented to the University of Waterloo
in fulfillment of the
thesis requirement for the degree of
Master of Applied Science
in
Electrical and Computer Engineering

Waterloo, Ontario, Canada, 2022

Author's Declaration

I hereby declare that I am the sole author of this thesis. This is a true copy of the thesis, including any required final revisions, as accepted by my examiners.

I understand that my thesis may be made electronically available to the public.

Abstract

Benign Prostatic Hyperplasia (BPH) is a noncancerous urologic condition in aging males where an overgrowth of the prostate gland occurs. It notably leads to lower urinary tract symptoms ranging from inconvenient nocturia to severe damage of the bladder from blockage, infection, and bladder stones. High-frame-rate ultrasound (HiFRUS) has enabled significant advances in urology through visualization of high temporal urinary flow dynamics within the male urinary tract during voiding. Such work has shown that characteristic flow patterns for pathological states found within the diseased male urinary tract, such as urethral obstruction, can be used for non-invasive assessment. However, complementing urinary flow are pressure wave dynamics propagating locally along the urethral tissue wall that has not been studied before. Here HiFRUS is utilized again to visualize and study in-vitro these local dynamics for a new metric to assess the male urinary tract state called the pressure wave velocity (PreWV). This research presents the first investigation on how significant the initiation of voiding in the collapsed and tortuous geometry of the urinary tract, which is common to BPH, are on the regional and subregional PreWV response.

A new tortuous flow phantom platform was devised to facilitate an in-vitro urodynamic study to collect PreWV data using HiFRUS and perform tissue Doppler analysis. To study the effect in changing the tortuous geometry, the male urinary tract is modelled by two deformable bent geometry phantoms, one with 30° bend and another with 45° bend. These phantoms were fabricated using a lost-core strategy protocol. To study the effect in changing the collapsed state, the phantoms were deflated and encased in a tissue mimicking slab where the opening of the collapsed lumen was controlled in a flow circuit setup. In this setup, initiation of voiding by a diseased patient was mimicked with a flow pump set at 15% duty cycle, 7 mL/s peak flow rate and 4 second period. HiFRUS imaging views near the inlet, at the bend, and near the outlet in each phantom were acquired through plane-wave imaging using a 192-channel linear array transducer connected to an ultrasound open research platform. Tissue Doppler analysis was employed on the beamformed frames to obtain the arrival times of the wall velocity at each lateral position in 0.1 mm lateral steps along the segmented phantom walls. Global PreWV results from this analysis were validated with the ground truth PreWV measured by pressure sensors that were connected to the inlet and outlet ports of the imaging setup. Regional and subregional PreWV results were validated through statistical analysis and agreed with theory regarding pressure wave propagation in human tissue.

For both the 30° and 45° phantoms, no statistical significance was observed on the PreWV near the inlet and outlet when compared to the ground truth ($p>0.14$; $N=11$). The subregional PreWV after the bend site showed a relative decrease in PreWV of 44% and 58% for the 30° and 45° phantoms respectively when

compared to the subregional PreWV before the bend ($p<0.001$; N=11). Furthermore, a noticeable difference in the bend regional PreWV was observed when comparing the 30° and 45° phantoms ($p<0.001$; N=11). It was found that a 15° increase in the phantom bend angle translated to 4 times increase in the difference between the subregional PreWV before and after the bend, thus highlighting the significance of the tortuous and collapsed geometry effects on the PreWV mapping. Overall, this work establishes PreWV as a novel metric to assess the urinary tract at sub-millisecond temporal resolution using HiFRUS and may serve as a complementary method to non-invasively distinguish pathological states due to BPH in future urodynamic studies.

Acknowledgements

I would like to thank my supervisor Professor Alfred Yu for all his efforts, patience, and guidance throughout my research and study. Thank you for this opportunity to study in the LITMUS lab at the University of Waterloo. To my lab members, thank you for sharing this experience with me.

I would also like to thank my family for their continued support and unwavering belief in me. I would not be where I am today without them.

Lastly, I would like to thank my two cats, Luna and Squash, for their entertainment and emotional support.

Table of Contents

List of Figures

List of Tables

List of Abbreviations

1-D	One dimension
2-D	Two dimensions
3D	Three dimensions
AUA	American urological association
B-mode	Brightness mode
BPE	Benign prostatic enlargement
BPH	Benign prostatic hyperplasia
BOO	Bladder outlet obstruction
C	Celsius
cc	Cubic centimeter
cm	Centimeter
CAD	Computer-aided design
CT	Computed tomography
CE-UroVPI	Contrast-enhanced urodynamic vector projectile imaging
dB	Decibel
FR	Frame rate
HiFRUS	High-frame-rate ultrasound
HRI	High-resolution image
Hz	Hertz
LRI	Low-resolution image
LUT	Lower urinary tract
LUTS	Lower urinary tract symptom
M	Million
MD	Doctor of medicine
MHz	Megahertz (10^6 Hz)
mm	Millimeter
mL	Milliliter
M-mode	Motion mode
MRI	Magnetic resonance imaging
m/s	Meter per second
PURR	Passive urethral resistance relation
PreWV	Pressure wave velocity

PRF	Pulse repetition frequency
PLA	Polylactic acid thermoplastic
PVA	Polyvinyl alcohol
RF	Radio frequency
SA	Synthetic aperture
TRUS	Transrectal ultrasound
URR	Urethral resistance relation

List of Symbols

Δ	Delta (variation)
λ	Lambda (wavelength)
ν	Nu (Poisson ratio)
ρ	Rho (density)
θ	Theta (beam-to-flow angle)
A	Cross-sectional area
c	Speed of sound
C	Compliance
D	Diameter
D_A	Distensibility of the vessel/tube
E	Yong elasticity modulus
f	Frequency
h	Wall thickness
I	Intensity
N	Number of transmissions
P	Pressure wave
P_b	Backward pressure wave
P_f	Forward pressure wave
Q	Volumetric flow rate/Flow velocity wave
Q_b	Backward flow wave
Q_f	Forward flow wave
R	Resistance
t	Time
v	Velocity of the blood cells
V	Velocity of the fluid
V_x	Lateral velocity
V_y	Axial component of velocity
W	Power
x	Distance

CHAPTER 1: INTRODUCTION

1.1 Chapter Overview

This thesis research is related to non-invasive monitoring of disease progression in the lower urinary tract system of male patients suffering symptoms of Benign Prostatic Hyperplasia. This chapter highlights some key aspects of the male urinary tract with prostatic gland where this disease develops and how this disease is diagnosed. This chapter also gives an outline of the thesis study including the motivation and hypothesis as well as research objectives.

1.2 Clinical Background

The field of male urology has suffered from clinical misdiagnosis due to a lack of non-invasive diagnostic tools that can provide accurate metrics for urology pathology. Thus, for the purpose of highlighting the ongoing research needs in this area, it is of scientific importance for researchers in the field of biomedical ultrasound to understand the clinical need for ultrasound flow imaging through its innovations in relation to urology. The following sections describe the diseases in the male urinary system and how they can be diagnosed using urodynamic imaging.

1.2.1 Urinary Tract Physiology

The focus of this thesis research is related to imaging disease progression in the male lower urinary tract; therefore, it is important to know the physiology of the lower urinary system which includes the kidneys, ureters, bladder, and urethra among others. The function of the urinary system is to filter blood and create urine as a waste by-product. Foods consumed that are protein rich are eventually broken down in the human body as liquid waste, which is called urea. Urea is carried in the bloodstream to the kidneys, where it is removed along with water and other wastes in the form of urine. Two narrow tubes called ureters carry urine from the kidneys to the bladder, which is a triangle-shaped, hollow organ located in the lower abdomen. At the bladder outlet, there is a circular muscle called the sphincter that helps keep urine from leaking out of the bladder. The bladder walls relax and expand to store urine. When it is time to urinate, the brain signals the bladder muscles to contract and flatten to expel urine out of the bladder, and at the same time, the brain signals the sphincter muscles to relax to let urine exit the bladder through a narrow tube called the urethra which allows urine to pass outside the body. When all the signals occur in the correct order, normal urination occurs.

The physiology of the lower urinary tract differs significantly between females and males. In the case of a male, there is a gland called the prostate, which is located just below the bladder, for the purpose of human reproduction. Zhang *et al.* (2013) thoroughly investigated human prostate size for different men aged from 40 to 70 years. In general, a normal prostate gland has an approximate size of 3 × 3 × 5 cm or a volume of 25 mL (Mitterberger *et al.*, 2010) and it surrounds a part of the urethra as shown in Fig. 1.1.

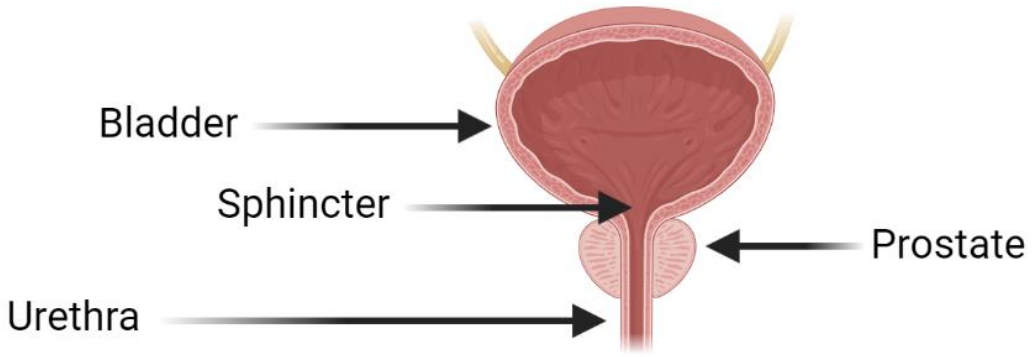

Fig. 1.1. Normal prostate in the lower male urinary tract.

1.2.1.1 Urinary Tract Disease - Benign Prostatic Hyperplasia

With age, the prostate tends to increase in size which can cause the urethra to narrow and decrease urine flow. This is called Benign Prostatic Hyperplasia (BPH), which is a Lower Urinary Tract Symptom (LUTS), but it is not the same as prostate cancer. The prostate consists of glandular and connective tissues and once these tissues expand it causes the urethral walls to stiffen thus narrowing the lumen of the tube. Fig. 1.2 shows enlarged prostate glands which are seen further narrowing the urethra.

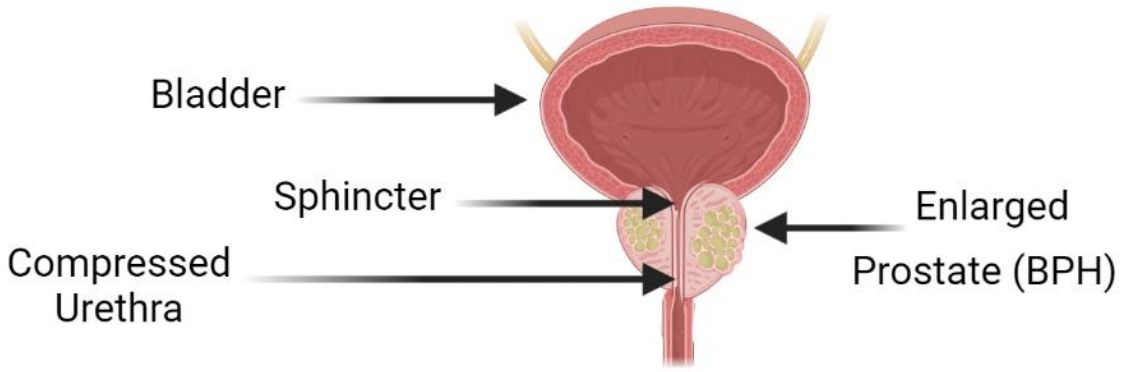

Fig. 1.2. Enlarged prostate with BPH showing compressed tube of the urethra.

Approximately 90% of men between 45 and 80 years of age experience LUTS, and more than 50% of men over the age of 60 years and 90% of men over the age of 70 years have symptoms related to BPH (McVary, 2006; Futterer *et al.*, 2008; Wasserman, 2006). Symptoms of BPH can include slow/dribbling urine flow and frequent urination with urgency. If left untreated BPH can also cause secondary problems which are more serious, such as an unexpected block in the urethra making it impossible to urinate, infection, stone in the bladder, blood in urine and even kidney damage because of back pressure from the overloaded bladder. Although BPH is not an immediately life-threatening disease, its impact on quality of life is substantial (Wei *et al.*, 2005), and therefore, its assessment for disease progression is necessary to know when treatment is necessary (O'Leary, 2000).

As mentioned earlier, most older men have symptoms related to BPH, this is because of changes in the geometry and elastic properties of the prostate. The human body contains tissues that are elastic in nature. When compressed, tissues undergo deformation that can be related to the stress-strain phenomenon (Fung, 1981). Tissues can be stiff or soft depending on their mechanical activities and the microscopic/macroscopic structure of their molecules. It was found that changes in tissue stiffness is related to diseases like prostate and breast cancers (Fung, 1981; Anderson, 1953). This was demonstrated by Zhang *et al.* (2008) who conducted stiffness measurement studies of ex vivo prostate tissues.

1.2.2 Diagnosis of Benign Prostatic Hyperplasia

The gold standard for bladder outlet obstruction studies the pressure flow urodynamic for bladder outlet obstruction which is used to diagnose BPH (Nitti, 2005). This method suggests that when the urethral

resistance (impedance) is higher, the pressure is higher. For the same resistance, the higher the pressure, the lower the flow, and vice versa as shown mathematically in Eq. 1-1.

$$R = \frac{P}{Q} \tag{1-1}$$

Where R is the resistance, P is pressure, and Q is the flow rate. Different researchers have developed different methods, such as urethral resistance relation, URR (Griffiths, 1973) and passive urethral resistance relation, PURR (Schafer, 1983 & 1985) to evaluate urethral resistance, however, those methods needed invasive urodynamic testing. Early research on the non-invasive measurement of pressure and flow used different techniques, such as using an external condom catheter (Schafer *et al.*, 1994), and a penile compression cuff (McRae *et al.*, 1995) to diagnose impediments in the urethra. However, those techniques failed because of leakage from condom and cuff release problems (Blake & Abrams, 2004). Considering the limitations of the gold standard, in this thesis research, the concept of pressure wave velocity (PreWV) has been introduced to diagnose BPH non-invasively using ultrasound imaging.

It has been reported that ultrasound is used to measure the size of the prostate (Pate *et al.*, 2020; El-Zawahry *et al.*, 2016). Krouskop *et al.* (1987) first used the Doppler ultrasound for non-invasive measurements of the mechanical properties of soft tissue while evaluating the connection of a prosthetic socket with a patient's residual limb. As mentioned in the previous section, changes in tissue stiffness may cause diseases in the prostate or breast, it is necessary to assess the stiffness for different tissue types, which can be done qualitatively and quantitatively. The qualitative assessment uses palpation or standard ultrasound; however, these techniques may not detect small-size lesions in the breast or prostate (Choyke, 1995; Garra *et al.*, 1997). Research on developing new imaging modalities has been underway in the last several decades to quantify the stiffness since quantification of the morphology of soft materials, such as stiffness changes in soft tissue, may provide valuable diagnostic information in the early detection of disease. One of the imaging technologies used to quantify tissue stiffness is elastography, which creates a visual map showing the stiffness of soft tissue. This medical imaging technology was first described in the 1990s by Gennisson *et al.* (2013). The basic principle of this modality is to apply a small amount of force to the tissue and record the deformation of tissue materials through a greyscale image called an elastogram. This force (per unit area) refers to the stress and the deformation is called the strain. The ratio of stress to strain is called the elastic moduli and it is determined from the initial slope of the stress-strain curve (Sigrist *et al.*, 2017).

Krouskop *et al.* (1998) studied image variations in elastography of prostate tissues whilst under compression to determine the elastic moduli and then consequently diagnose diseases. In their study, a total of 113 prostate tissue samples were tested, which included 32 samples of the normal anterior portion of the gland, 32 from its normal posterior portion, 21 from BPH, and 28 from cancerous tissues. It was found that the order of stiffness of different tissue types in the prostate is as follows:

$$\text{BPH} << \text{Normal Anterior and Posterior} << \text{Cancer}$$

Despite the overgrowth of the prostate gland that in turn compresses the urethral wall, these research findings suggest that the prostatic tissue has become less stiff for males with BPH symptoms.

Other studies have used vector flow for imaging the urinary flow dynamics in a bladder outlet obstruction model where an increase of 0.91 m/s from the baseline 1.43 m/s spatial-max flow of the normal model was observed (Ishii *et al.*, 2017). While BPH is known to be a progressive condition for the aging male, fully realizing the severity and occurrence of it typically requires knowledge of the complex fluid flow dynamics of the bladder, bladder neck, prostate, and urethra, which are poorly understood due to a lack of convenient and patient comfortable diagnostic technology (Foster *et al.*, 2018). Hence, urodynamic evaluation and imaging are areas of great interest.

1.3 Outline of Thesis Study

1.3.1 Motivation and Hypothesis

BPH is a non-cancerous condition in aging males where an overgrowth of the prostate gland occurs. It notably leads to LUTS ranging from inconvenient nocturia to severe damage of the bladder from blockage, infection, and bladder stones (Thorpe, 2003; Vos *et al*., 2016; McVary, 2006; Wei *et al.*, 2005). BPH manifested by bladder blockage can be imaged using conventional ultrasound; however, this diagnosis does not provide quantifiable and reliable metrics. The clinical gold standard is an invasive urodynamic test that measures pressure changes within the male bladder to objectively indicate the severity of BPH (Nitti, 2005; Edwards, 2008). A 2019 BPH clinical guidelines review highlighted that the information gained from urodynamic testing is limited as it does not quantify the progression of the drivers behind BPH, and the invasiveness of the procedure posed the risk of potential damage to the urethra in practice. Consequently, there is a clinical need to devise a safe patient-friendly diagnostic method to quantify the extent of BPH progression (Foster *et al.,* 2018; El-Zawahry *et al.*, 2016; Mehdizadeh & Leach, 2009). High-Frame-Rate Ultrasound (HiFRUS) can be leveraged to address this need.

This thesis is broadly based on the hypothesis that HiFRUS, with its sub-millisecond time resolution, can be harnessed to accurately quantify the symptom of BPH, hence a new set of engineering innovations for HiFRUS-based urodynamic monitoring are proposed as future research directions. The proposed innovations are expected to stepwise progress from algorithmic design to *in-vitro* testing and *in-vivo* application in several stages, however, as an initial part of this overall innovation, in this research a phantom modelling of the male urinary tract anatomy for PreWV validation is conducted.

HiFRUS has enabled significant advances in urology through visualization of high temporal urinary flow dynamics within the male urinary tract during voiding. Such work has shown characteristic flow patterns for pathological states found within the diseased male urinary tract, such as urethral obstruction, to assess these disease states non-invasively (Ishii *et al.*, 2020; Ishii *et al.*, 2017). However, complementing urinary flow are pressure wave dynamics propagating locally along the urethral tissue wall, which has not been studied before. In this research, HiFRUS is utilized to visualize local urodynamics and study *in-vitro* a new metric to assess the male urinary tract state called the PreWV. The male urinary tract can be decomposed into separate phantoms, each modelling a key feature out of the three present in a BPH diseased urethra: 1) stiffness resulting from urethral obstruction, 2) collapsed state of the tract lumen, and 3) the tortuous geometry of the urethra. Specific to this work, it is hypothesized that these three features are significant to calibrate PreWV mapping response along the urinary tract for translating this work from *in-vitro* experimentation to an *in-vivo* study. However, this study focuses on phantom models of features 2) and 3), which are the collapsed state and the tortuous geometry state respectively. Validation of the HiFRUS measured PreWV response from these phantoms is done with a differential pressure transducer acting as the ground truth. Statistical analysis is done to quantify the significance of these features on the PreWV response as part of the modelling of the urinary tract anatomy. By the end of this research, there will be a reproducible protocol to validate the performance of PreWV of the urinary tract *in-vitro* for urology researchers to build upon.

1.3.2 Research Objectives

The overall objective of this research is to non-invasively visualize and quantify urological dynamics at fine temporal resolution by devising a new HiFRUS imaging framework that involves PreWV principles. This imaging framework could be applied for future urodynamic monitoring to measure urethral stiffness that is derived from the measurement of PreWV localized along the urinary tract in male patients suffering from BPH.

CHAPTER 2: MOTION IMAGING WITH ULTRASOUND

2.1 Chapter Overview

In this research, real-time imaging using HiFRUS methods has been used for motion estimation in the lower urinary tract to diagnose diseases related to BPH. This chapter describes the basics of ultrasound, the fundamentals of ultrasound imaging, and Doppler-based motion estimation including the techniques of HiFRUS.

2.2 Ultrasound Imaging Basics

Ultrasound is a form of sound with a frequency that is above the range of human hearing. A healthy human can hear a sound if it is in the range of 20 cycles per second or Hertz, abbreviated as Hz, to 20,000 Hz. If the frequency of a sound is less than 20 Hz or more than 20,000 Hz, it cannot be heard by humans and is referred to as infrasound or ultrasound, respectively. The fundamental of ultrasound imaging is based on a simple phenomenon known analogously as an echo system. Ideally, when sound waves are emitted towards a solid object at a right angle, they are reflected back towards the emitter with a time delay. If the time delay corresponding to the back-and-forth distance is known, dividing it by the speed of sound can give the distance of the echogenic object.

2.2.1 Physical Principles

Sound is a mechanical wave, and it can only travel through a medium, hence matter must be present for sound to travel, which explains why sound cannot propagate through a vacuum. Sound is categorized according to its frequency, which is the number of mechanical variations occurring per unit of time. As mentioned above, the human audible range is 20 – 20000 Hz, whereas diagnostic ultrasound ranges from 1–20 MHz (Chan & Perlas, 2011). Typical frequencies used in medical ultrasound are 2–10 MHz (Abuhamad, 2014). The characteristics of a sound wave can be described by the following parameters:

Period (T) – the time taken for a particle in the medium through which the wave is traveling to make one complete oscillation about its rest position. One oscillation is also known as a cycle.

Frequency (f) – the number of cycles per second performed by the particles of the medium in response to a wave passing through it. Expressed in Hertz, where 1 Hz = 1 cycle passing a given point each second.

Wavelength (λ) – the distance between two consecutive, identical positions in the pressure wave, which is determined by the frequency of the wave and the speed of propagation in the medium through which it is

traveling. Frequency and wavelength have an inverse relationship. Table 2.1 shows the frequencies and their respective wavelengths generally used for soft tissue ultrasound imaging.

Table 2.1. Frequencies and their wavelengths for soft tissue.

Frequency (MHz)	**Wavelength (mm)**
3	0.51
5	0.31

Velocity (c) – speed of sound with direction specified. The speed of sound propagation is determined based on the density and compressibility factors of the medium through which the sound is traveled. Table 2.2 shows the speed of sound in different media (Abuhamad, 2014; LCMC, 2012).

Table 2.2. Speed of sound in different media.

Media	**Speed of Sound (m/sec)**
Air	330
Metal	5000
Pure Water	1430
Bone	4080

Speed of sound in various soft-tissue type organs of the body also differs as shown in Table 2.3.

Table 2.3. Speed of sound in various soft-tissue.

Soft-Tissue	**Speed of Sound (m/sec)**
Fat	1450
Liver	1550
Blood	1570
Muscle	1585

In practical terms, ultrasound machines need to operate on a single value for the speed of sound in soft tissue; therefore, an average speed for soft tissue is taken to be 1540 m/sec (LCMC, 2012).

Amplitude (A) – A maximum variation of an acoustic variable, thus amplitude is a measure of the degree of change within a medium when a sound wave passes through it and relates to the severity of the disturbance. In this way, the amount of energy in a sound wave can be determined. Amplitude is expressed in units that are appropriate for the acoustic variable considered.

Power (W) – The rate at which work is done or the rate of flow of energy through a given area. In diagnostic ultrasound energy is contained within the beam, so the power is the rate of flow of energy through the cross-sectional area of the beam. Power is expressed in Watts.

Intensity (I) – Power per unit area. Intensity is expressed in milliwatts per square centimeter (mW/cm^2). Intensity is an important parameter in describing an ultrasound beam and in the understanding of bioeffects and safety.

Ultrasound imaging uses an ultrasound beam, which is produced based on the principle of piezo-electricity which mentions that when pressure is applied to some materials it deforms and produces a voltage, and when a voltage is applied it deforms and produces a pressure. The applied voltage to the faces of an artificially made crystal expands or contracts the crystal depending upon the polarity of the voltage applied. The crystal then resonates (rings), converting electricity to ultrasound. The frequency of the sound produced is dependent on the thickness of the crystal. On the other hand, when the crystal receives an echo,

the sound deforms the crystal, and a voltage is produced on its faces. This voltage is then analyzed by the system to produce an image.

During ultrasound imaging, a transducer (probe), which includes a case, crystal component, and damping materials connected to the ultrasound system by electrical wiring, produces and receives the pulses of sound. Most real-time transducers use multi-element transducers containing many small crystal elements for the formation of each pulse. This type of transducer is also known as a linear array transducer where each individual element is acoustically and electrically isolated, allowing flexibility in beam formation. The ultrasound beam width is important to the spatial image quality produced (LCMC, 2012). All sound beams are three-dimensional. Fig. 2.1 shows a schematic of the beam profile of a simple transducer, which shows that the energy is not confined to a single lobe, but it produces side-lobes by "off-axis" energy that surrounds the primary beam. Array transducers also generate weaker beams called grating lobes when sound energy travels out in different directions from the primary beam because of the multi-element structure of transducer arrays. Although both side lobes and grating lobes can be minimized by proper designing of a transducer, still there could be artifactual echoes resulting in images that do not accurately reflect the anatomy of the scan plane.

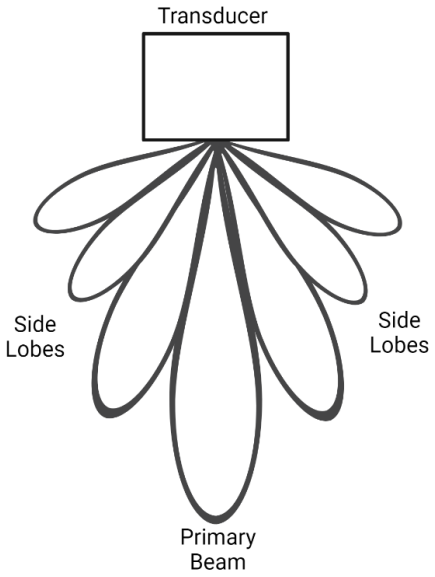

Fig. 2.1. Beam profile of a simple transducer.

To produce high-quality images, good resolution is necessary. Generally, resolution is distinguished by the timing and magnitude of received echoes and is characterized further below:

1. **Contrast Resolution:** The ability of an ultrasound system to demonstrate the differentiation between tissues having distinctive characteristics e.g., liver/spleen.
2. **Temporal Resolution:** The ability of an ultrasound system to accurately show changes in the underlying anatomy over time, this is particularly important in echocardiography.
3. **Spatial Resolution:** The ability of the ultrasound system to detect and display structures that are close together. Spatial resolution can be axial and lateral. This resolution is particularly important in medical ultrasound where the image needs to display the depth and width across a section of anatomy in a human patient.

In medical ultrasound, when a sound beam passes through tissues within the body, it loses energy and therefore undergoes a reduction in amplitude and intensity which is called attenuation. The amount of attenuation is determined by the tissue involved, the distance traveled, and the frequency of the beam. Four main factors affect the echoes returning to the transducer as well as the transmitted beam. Those factors are:

Reflection: This occurs at interfaces between soft tissues of differing acoustic impedance, i.e. the degree of impedance mismatch. The percentage of the sound reflected is dependent on the magnitude of the impedance mismatch and the angle of approach to the interface. For instance, in the case of soft tissue/air interface - 99.9% reflected, for soft tissue/bone - 40% reflected and for Liver/Kidney - 2% reflected (LCMC, 2012).

Refraction: When the path of a beam deviates through interfaces between tissues of differing speeds of sound, refraction occurs. Refractions can produce some artifacts.

Absorption: When an ultrasound beam passes through the material, some of the energy of the beam is transferred to the material which is called absorption. It accounts for most of the wave attenuation. Absorption increases with frequency, and it produces a heating effect.

Scattering: Within the sound beam path scattering occurs at interfaces.

Since ultrasound is a form of mechanical energy, the quality of produced images depends on their output based on the mode applied. During diagnostic ultrasound, different mode techniques are used as described below:

A-mode (Amplitude mode): In A-mode, the amplitude and depth of a single received ultrasound echo is tracked over time and plotted in a graph. Historically, A-mode ultrasound was used in obstetrics in measuring biparietal diameters, however, it is no longer used in clinical practice (Abuhamad, 2014).

B-mode (Brightness mode): This commonly used modality displays a two-dimensional spatial image by mapping the multiple echoes that are received from the simultaneous firing of an array of sound emitters. B-mode images are obtained in real-time, and these images are displayed in greyscale format.

M-mode (Motion mode): M-mode originates from displaying a single vertical slice of the B-mode image and then tracking the motion of this image slice over time. The motion is updated based on the pulse repetition frequency. In practice, ultrasound technicians do not employ this mode frequently unless it is for assessing the motion of fetal cardiac conditions (Abuhamad, 2014).

2.2.2 Doppler Based Motion Estimation

A Doppler ultrasound is an imaging technique that uses sound waves to show moving objects, such as blood moving through blood vessels. While a regular ultrasound can create images of structures inside the body, it cannot show blood flow. Doppler ultrasound works based on *Doppler principle*, which was developed in 1843 by a physicist named Christian Doppler, to explain a change in the perceived frequency of sound emitted by a moving source (Moorthy, 2002). There are several types of Doppler, such as:

- **Color Doppler:** This type of Doppler uses post-processing to convert sound waves into distinct colors for indicating the direction of movement. Color Doppler mode is superimposed on the real-time B-mode image to detect the presence of flow. By convention, if the flow is towards the transducer, it is colored red, and if the flow is away from the transducer, it is colored blue.

- **Power Doppler**: This is an alternative type of color Doppler based only on the magnitude of the acquired sound waves. It can provide more detail of blood flow than the standard color Doppler. However, it cannot show the direction of blood flow. Power Doppler mode is helpful in the detection of low-velocity flow where color Doppler may not be able to display such flow properly.

- **Spectral (Pulsed) Doppler.** This Doppler mode records changes in flow speed at a specific region in the image and reports them in a spectrogram. Flow moving towards the ultrasound probe has its speed reported above a baseline, while flow moving away from the probe has its speed reported below this same baseline.

- **Continuous Wave Doppler.** In this technique, sound waves are sent and received continuously with two probes, which allows for more accurate measurement of flow moving at faster speeds.

Historically, research in ultrasound motion estimation began when the Doppler ultrasound flow imaging technique was developed. In the past, researchers made significant progress in ultrasound imaging

of blood flow. Satomura (1957) is the first to have invented a flow imaging method in the late 1950s to detect fluid flow patterns within humans using a continuous wave ultrasound system with two probes. A decade later, another researcher developed a pulsed wave ultrasound system that could display the spectral content of the flow signals with a single probe (Baker, 1970). Within a limited spatial location, both systems could estimate flow in one dimension (1-D). Since then, advanced techniques such as vector flow imaging have been developed and have advanced biomedical ultrasound research for flow estimation. This section discusses some techniques for flow estimation made available during the beginning of ultrasound flow imaging, such as pulse Doppler and crossbeam vector Doppler ultrasound, as well as their limitations.

2.2.2.1 Pulse Doppler Ultrasound

In 1957 the first record of Doppler ultrasound flow imaging was published (Satomura, 1957). It is assumed that the Doppler effect is used to estimate the motion of interest within the medium being flooded with sound waves, as ultrasound uses the nature of sound to display flow information. Usually, groups of red blood cells are targeted due to how echogenic they are and if the flow is disturbed within the blood vessel, this could indicate that a form of vascular pathology is present within the blood vessel (Satomura, 1959; Sigel *et al.*,1983). The sound waves would be transmitted by a transducer and interactions between the blood cells and sound waves would cause the sound waves to scatter which would then be picked up by the receiving transducer. If a single transducer is used for both transmitting and receiving then the Doppler shift frequency (f_d) from a single transmitted pulse is calculated using Eq. 2-1 (Jensen, 1995).

$$f_d = f_r - f_o = \frac{2vf_o \cos(\theta)}{c} \tag{2-1}$$

Here f_r is the frequency of the received signal, f_o is the frequency of the sound pulse transmitted by the transducer, θ is the beam-to-flow angle, c is a constant for the speed of sound, and v is the flow velocity of the blood cells. Although Eq. 2-1 is known as the Doppler shift for a pulse wave, it is not derived based on Doppler principles. The relation is raised from the phase change between the transmitted and received signals. As well, the samples between pulse firings, which are set by the pulse repetition frequency (PRF), are used to determine, and update the flow velocity of a target of interest at a specific depth. This technique is known as pulse Doppler flow estimation.

Although pulse Doppler paved the way for ultrasound flow imaging, three major problems were noted that hindered its clinical diagnostic value: flow dimensionality, beam-to-flow angle inaccuracies, and framerate limitations arising from sequential beamline transmission. Eq. 2-1 only tracks motion flowing towards or away from the transducer, as $v\cos(\theta)$ gives the axial velocity component of a moving target.

This is an issue as limited diagnostic information is given because flow moving laterally relative to the transducer surface that could display irregular flow patterns to a clinician would not be observable (Jensen, 1995). Secondly, in practice, the beam-to-flow angle is assumed to be 60 degrees as it is too difficult to measure. This not only introduced inaccuracies in calculating the flow velocity but also caused limitations in visualizing the flow components perpendicular to the transmitted beams. Lastly, the framerate to which the velocity of flow can be calculated is limited by the number of scanlines and the PRF. This is due to the velocity being updated between every repeated pulse firing from the transducer and the PRF being set by the user controlling the ultrasound. This limitation of framerate between sequential firings also restricts the range of flow velocities that could be viewed at a time, presenting again a diagnostic limitation for the need to visualize flow outside this range.

2.2.2.2 Crossbeam Vector Doppler Ultrasound

Crossbeam vector Doppler ultrasound for angle-independent velocity measurements is a technique that reduces the number of beamlines needed to produce vectors (Dunmire *et al*., 2000). The two-dimensional (2-D) velocity estimates are obtained by combining two independent 1-D velocity estimations. This is realized along two steered beamline transmissions that cross each other for calculating both vector components.

First suggested by Fox (1978), the echo graphic system with two crossing beams estimates the lateral velocity component by triangulation. This system went through further optimization (Dunmire *et al*., 2000), however, due to the architecture of this transmission scheme, the two beams had to be placed far apart. This led to difficulties in imaging flow in deep areas surrounded by tissue. Furthermore, this procedure would need to be carried out for all moving targets within the insonified view, causing the framerate to be low. The framerate issue that held back traditional flow estimation could not be fully addressed until the 21st century when modern flow estimation techniques existed by utilizing transmission schemes and advanced computing hardware, which had faster processing capabilities (Tanter, 2014; Yiu *et al.*, 2011; Hansen *et al.*, 2011).

2.3 High-frame-rate Ultrasound

With new imaging modality advancements, conventional techniques such as scanline B-mode imaging are outdated and not sufficient for fast flow visualization at a high temporal resolution. Researchers have proposed over the years of using high-frame-rate ultrasound (HiFRUS) for real-time imaging systems (Loizou *et al.*, 2018; Jensen, 2007; Tanter & Fink, 2014; Boni *et al.*, 2017). There are benefits from conventional ultrasound, for example, it offers many imaging modes for quantitative and qualitative

evaluation (Otto, 2012), however, there are also limitations such as the current achievable frame rate, which is about 30 - 40 Hz (Montaldo *et al.*, 2009). Some clinical applications such as stress echocardiography with 120-140 beats/minute (Marwick, 2003), fetal echocardiography with 120-170 beats/minute (Weerakkody & Jones, 2022), visualization of fluid flow in the urinary system or coronary arteries, need a higher frame, which can be calculated based on Eq. 2-2.

$$FR = \frac{PRF}{N_{TX}} \tag{2-2}$$

Where *FR* is the frame rate, *PRF* is the pulse repetition frequency of the transmissions, and N_{TX} is the number of transmissions.

High-frame-rate ultrasound can form a B-mode image by insonification of a large area with unfocused beams, such as plane waves or spherical waves (Au *et al.*, 2018). Also, strain and strain rate could be improved by a higher temporal resolution. Different researchers tried different methods to improve HiFRUS. Podkowa *et al.* (2018) studied high-framerate Doppler ultrasound using a repeated transmit sequence where they were able to record an axial velocity for a range of 300 mm/s.

A technique called Synthetic Aperture (SA), which was originally proposed for radar in the early 1950s, was later investigated in ultrasound imaging (Burckhardt *et al.*, 1974; Johnson *et al.*, 1975). This process involves the rapid firing of low-energy unfocused waves on transmit, as well as performing receive focusing to achieve a high framerate. This improves the peak range flow estimation significantly compared to traditional methods. The receive-focusing procedure involves combining low-resolution images (LRI) formed from each unfocused firing, which is a spherical or plane wave, to produce a high-resolution image (HRI) (Jensen *et al.*, 2006). The following section describes some aspects of this technique:

1) Spherical Waves: The unfocused firings can originate from the placement of a virtual point source near the transducer which activates a group of elements per emission. This is useful for increasing the signal strength of the received LRIs. Also, the firings can be from a single element of the transducer. In both cases, when the elements at the ends of the transducer are in an alternating pattern the transmission becomes optimal for flow estimation

Fig. 2.2 shows the signal level waveforms along the same direction. The *n*th generated HRI is cross-correlated in the time domain to determine the shift with another HRI signal that is separated by *n–N* emissions. The peak of these cross-correlations determines the velocity and can be averaged as they are all subject to the same time shift (Nikolov & Jensen, 2001).

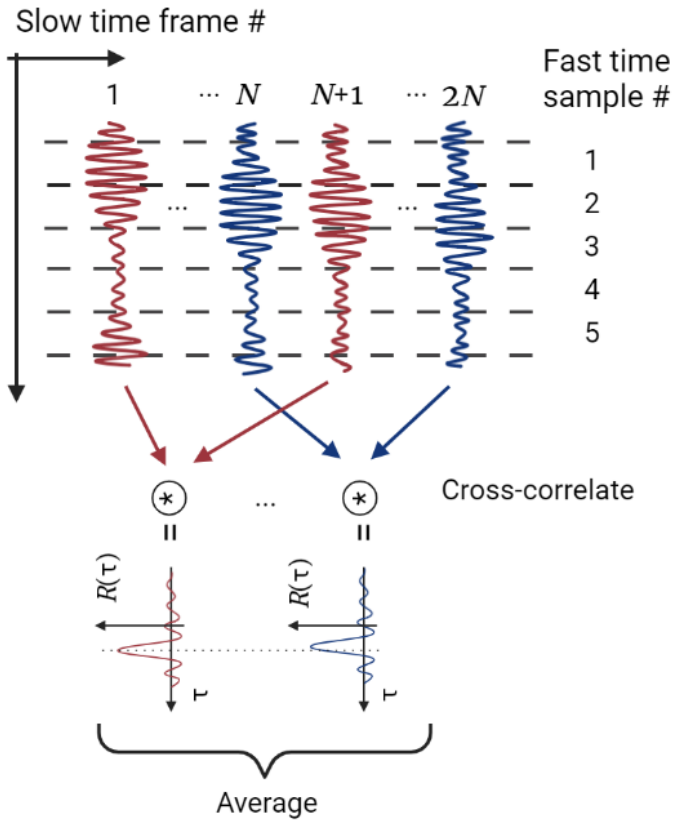

Fig. 2.2. Cross-correlation of HRIs to calculate the peak velocity mean.

Jensen *et al.* (2006) used the synthetic aperture method with dynamic focusing where a spherical wave using a single element of the transducer was transmitted and the echoes were then received using all the elements of the transducer. For each transmission-reception event, one LRI is obtained. By repeating this process for different elements in the transducer and combining all resulting low-resolution images, a HRI can be obtained as shown in Fig. 2.3.

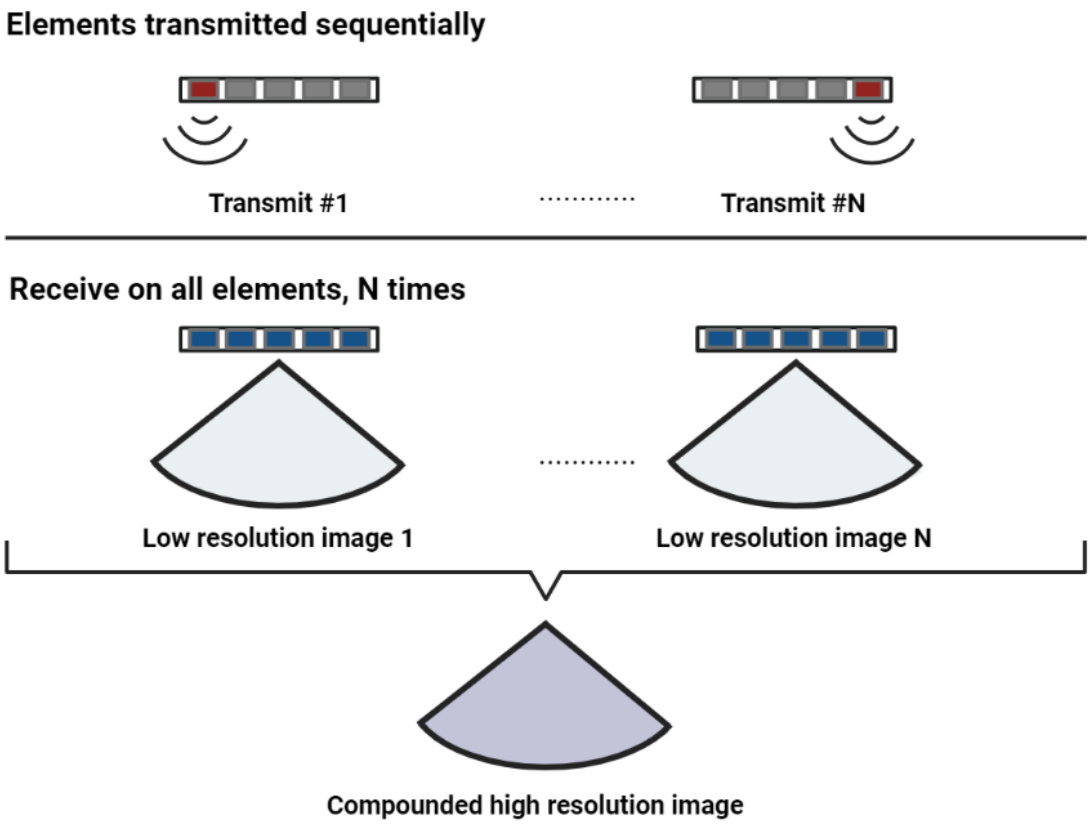

Fig. 2.3. Basic implementation of synthetic aperture imaging.

2) Plane Waves: LRIs are generated by having the whole region flooded with controlled sound waves which are projected from the transducer at different propagation angles of the wavefront. The wavefront has angles that are with respect to the surface normal of the transducer. HRI is used in flow vector calculations, and it is produced by compounded LRIs. In Fig. 2.4, the plane-wave transmission scheme can be seen where it is used to calculate the flow vectors. The solid and dashed line areas are where each component of the flow vector is obtained. The 2-D blood flow vector can be derived using geometric principles and compounding (Jensen, 2017).

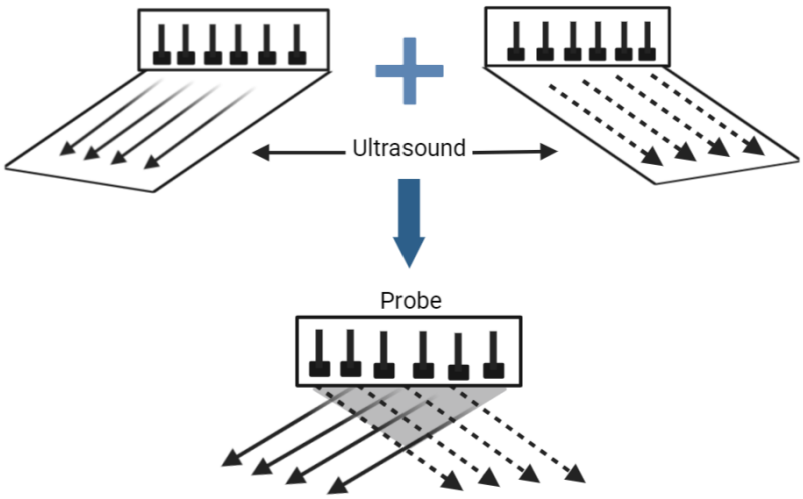

Fig. 2.4. Transmission scheme diagram of the 2-D vector flow using plane waves.

To calculate the 2-D motion vector within the field of view, Eqs. 2-3 & 2-4 are used (Masuno, 2014).

$$V_x = \frac{v_2 - v_1}{2 \sin \theta} \tag{2-3}$$

$$V_y = \frac{v_2 + v_1}{2 \cos \theta} \tag{2-4}$$

The 1-D components v_1 and v_2 are measured from the complement pair of positive and negative steered transmission angles, theta (θ), respectively. The calculated lateral velocity is the variable V_x while V_y is the axial component.

Note that accurate estimates of the velocity are limited to the grey-colored triangular area shown at the bottom of Fig. 2.4. Accuracy decreases with the velocity vectors outside the triangular area. To mitigate the limitation of accuracy, the strategy of combining different methods such as dual or multi-beam Doppler (Fox, 1978), Doppler spectral symmetry (Tortoli *et al.*, 2006), transverse oscillations (Jensen & Munk, 1998), and directional beamforming (Kortbek & Jensen, 2006) have been used.

In the medical science field, significant importance is given to measuring fluid velocity. A technique has been developed by researchers which improves blood quantification. The technique involves combining 2-D vector flow imaging and tracking Doppler methods which help reduce bias and fluctuations in maximum velocity measurements (Avdal *et al*., 2017). Aliasing resistant vector Doppler algorithm is used to estimate blood flow direction, which is then proceeded by the tracking Doppler method being applied to the same data. The tracking direction is estimated using the direction of the vector Doppler. Not only can vector flow imaging data provide fluid velocity measurements, but also flow complexity for

revealing disturbed and turbulent flow (Hansen *et al.*, 2016; Hansen *et al*., 2017), flow volume (Jensen *et al.*, 2014), and pressure gradients (Nguyen *et al*., 2019) can be derived from flow imaging data.

2.4 Chapter Summary

This chapter summarized different aspects of ultrasound and its uses for flow imaging in biomedical science. The Doppler-based motion estimation techniques included pulse Doppler and crossbeam vector Doppler. For modern flow imaging a fast and higher frame rate is necessary for qualitative and quantitative evaluation of disease progression in human beings. This chapter highlighted the advancement in HiFRUS technique that uses plane-wave imaging and synthetic aperture process, which combines LRIs formed from each unfocused firing to produce a HRI. With HiFRUS technique, both fluid velocity and flow complexity can be estimated.

CHAPTER 3: PRESSURE WAVE VELOCITY BASICS AND IMAGING

3.1 Chapter Overview

The novelty of this thesis research is to use the concept of pressure wave velocity (PreWV), where the pressure wave is increased because of a reflected wave caused by the impedance from BPH bladder outlet blockage as well as reflections in the tortuous geometry of the male urinary tract. There is limited literature present on applying a rudimentary idea of PreWV in urodynamics, but no urology literature to date has applied it in the specific manner described in this thesis. However, researchers have studied a similar method in cardiovasculature for imaging blood flow and measuring pressure in the artery, as the reflective wave generated in arteries with plaque and at the narrow portion of the peripheral artery provides impedance. Therefore, to make this concept clear, most literature review in this chapter is related to a model for the cardiovascular system that is similar to the fluid dynamics of the urinary system. This chapter details wave dynamics, such as the basics of forward and reflected waves, how PreWV characteristics similar to vascular pathology originate in BPH, and the methodology for imaging PreWV by estimating tissue motion with lag one autocorrelation. The use of phantoms to assess the performance of PreWV is also mentioned.

3.2 Wave Dynamics

PreWV is a new metric proposed for urodynamic imaging. A pressure wave is also known as a pulse wave. Only limited research has been carried out in the past on a basic form of this technique known as a urinary tract pressure flow study (Nitti, 2005), however, many researchers have studied a similar application of pressure and flow waves in the vascular system where blood flows from the heart to the network of blood vessels consisting of arteries, arterioles, capillaries, venules, and veins (Tarantini *et al.*, 2020; Pereira *et al.*, 2015; Calabia *et al.*, 2011; Rabben *et al.*, 2004; Fujikura *et al.*, 2007; Brands *et al.*, 1998; Nabeel *et al.*, 2020). The following sections describe the fundamentals of wave dynamics as this concept is used in this thesis research.

3.2.1 Pressure Wave Velocity Origins in Benign Prostatic Hyperplasia

As mentioned earlier, the urinary tract and arteries in the vascular system are composed of materials with viscoelasticity, which means that the material is not only elastic but also has viscous (fluid-like) properties. They are multilayered and nonlinear conduits that contain fibers like elastin and collagen in addition to tissue cells. Elastin fibers are the most distensible components while collagen fibers are stiffer. There is a relation between intraarterial pressure and arterial wall distensibility, and their waves have a

similar shape, hence, pulse wave velocity is a biomarker for the assessment of arterial stiffness. Bramwell & Hill (1922) found that the amount of arterial disease can be quantified from the measurements of wave velocity or the distensibility of the artery using the re-arranged Eq. 3-1 (Westerhof *et al.*, 2018).

$$c = \sqrt{\frac{A}{\rho C}} = \sqrt{\frac{A \cdot \Delta P}{\Delta A \cdot \rho}} \tag{3-1}$$

Where c is the propagation velocity of a pressure (or flow) wave, A is the cross-sectional area of the artery, ρ is the density of the blood, C is compliance, and $\Delta A/\Delta P$ is the local "cross-sectional compliance," expressing the distensibility of the artery. Elastance and compliance (pressure-volume relation) are the opposite of each other. The wave propagation velocity can be measured from time delay (Δt) between the feet of the wavefront in two locations at a distance Δx, and is expressed as $c = \Delta x/\Delta t$ (Luo *et al.*, 2012). Since the propagation velocity of pressure and flow wave is the same, a Doppler ultrasound recording of the flow wave at two distant locations allows the estimation of time delay between the feet of the wave. Therefore, the technique of elastography is an ultrasound-based method for imaging the deformation of the tissue motion or arterial wall motion (De Korte *et al.*, 2016).

In practice, it is convenient to characterize the vessel wall using the Yong elasticity modulus (E) as shown in Eq. 3-2.

$$E = \frac{\Delta P}{\Delta D} D^2 \frac{(1-\nu_p^2)}{2h} \tag{3-2}$$

Where, ΔD is the diameter variation corresponding to the pressure variation (ΔP), h is the wall thickness, and ν_p is the Poisson ratio of the wall material (0.5 for biological tissue) (Bergel, 1972). Other indices for characterizing the mechanical stiffness are the cross-sectional compliance (C) and the distensibility of the vessel (D_A) as expressed in Eqs. 3-3 & 3-4.

$$C = \frac{\Delta A}{\Delta P} = \frac{\pi D \Delta D}{2\Delta P} \tag{3-3}$$

$$D_A = \frac{\Delta A/A}{\Delta P} = \frac{2\Delta D}{D\Delta P} \tag{3-4}$$

Tissue stiffness is an adverse structure within the urethra or vascular walls (Teixeira *et al.*, 2016). It is known that plaques in arteries cause them to thicken and stiff the arterial wall making the flow passage narrow and altering the wall elasticity. As mentioned earlier, researchers found that the wave propagation

velocity increases with aging (Avolio *et al.*, 1983; O'Rourke *et al.*, 1968) because of stiffness or narrowing tube caused by artery plaques (Fig. 3.1), which is justified by the continuity equation (Eq. 3-5) of fluid mechanics (Munson *et al.*, 2006).

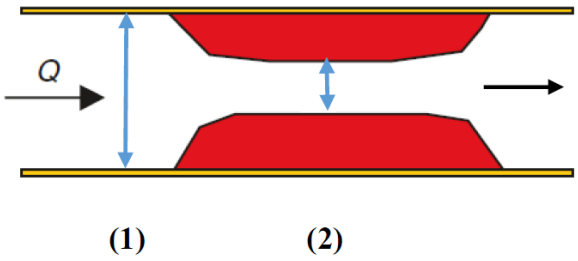

Fig. 3.1. Fluid flow in different sections of a tube. Section (1) is the original size of the tube lumen and section (2) is the narrow portion of the lumen.

$$Q = A_1V_1 = A_2V_2 \tag{3-5}$$

Where Q is the volumetric flow rate, A is the cross-sectional area of the tube, and V is the velocity of the fluid. Since A_1 is greater than A_2, to satisfy the continuity equation $V_2 > V_1$, i.e. fluid velocity is higher at the narrow inner passage of the tube because Q is constant in a continuous flow process. This is also the situation in Fig. 1.2 where the urethra is stiffened and the lumen of the urethra is decreased because of compression by the enlarged prostate gland that causes BPH and in that case, the urine flow is decreased because of blockage, which is similar to plaque in arteries. Most importantly, because of this restriction of urine flow at the prostate with BPH, there is a development of pressure wave reflection that is discussed in Section 3.2.2.

3.2.2 Forward and Reflected Waves

There are two types of waves, such as pressure wave and flow velocity wave, and each type of wave consists of two components of waves: forward and reflected waves. In both urodynamic and hemodynamic systems these kinds of waves are formed. For instance, in the cardiovascular system, when the heart pumps, pressure and flow waves are generated in the ejecting blood, which rhythmically travels along the arterial tree from the aorta to peripheral arteries. Systole occurs when the heart muscle contracts and pushes blood out of the heart. Whereas diastole is when the heart muscle relaxes, and the chambers of the heart are filled with blood.

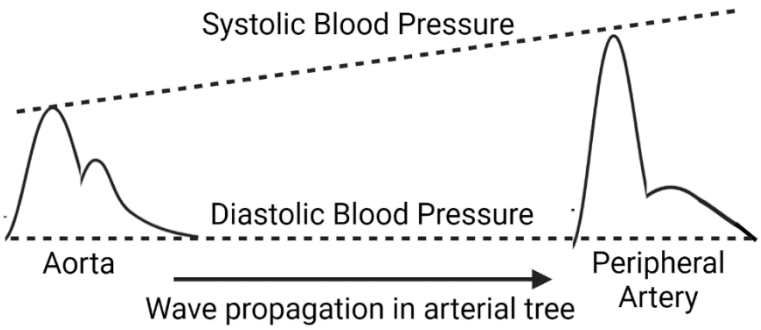

Fig. 3.2. Change in blood pressure values from the center to the periphery of the arterial system.

Fig. 3.2 shows the change in blood pressure values from the center (aorta) to the peripheral artery. It is important to observe that the systolic blood pressure is increased markedly in the peripheral artery and the wave peak becomes steeper. This is because of the wave reflection in the systemic vascular resistance at the peripheral arteries with capillaries (Salvi, 2017). The measured pressure waves consist of two components:

1) Forward Pressure Wave: This is the pressure wave away from the heart, which is also called an incident wave.
2) Reflected Pressure Wave: This is the pressure wave towards the heart, which is also called a backward wave.

The concept of wave reflection can be better explained in a simple example if we consider what happens when we drop a stone into the center of a basin full of water. Initially, the impact of dropping stone creates a concentric wave that propagates towards the edges of the basin (forward wave). When this wave hits the external edges, it creates a backward wave towards the center of the basin, which is the "reflected wave" like ocean waves breaking on the rocks and then going back to seaward. If we drop a series of stones, at regular intervals, we can see that the reflected/backward waves superimpose on the forward waves generating much larger waves, which is the result of increased pressure in the peripheral artery shown in Fig. 3.2.

In the absence of wave reflection, there is a linear relationship between blood pressure and flow velocity like watering a garden using a hose where the stronger the water pressure, the faster the water flows. However, in the presence of reflected waves, the relationship between pressure and flow waves is the opposite. In this case, the forward flow wave is suppressed by the reflected wave, which is reminiscent

of walking against the wind, where the wind will reduce one's walking speed. Hence, in the arterial system, the amplitude of the resultant wave can be defined as:

$$\text{Pressure Wave (P)} = \text{Forward Pressure Wave } (P_f) + \text{Backward Pressure Waves } (P_b)$$

$$\text{Flow Velocity Wave (Q)} = \text{Forward Flow Wave } (Q_f) - \text{Backward Flow Waves } (Q_b)$$

The difference between the pressure wave and flow velocity wave in the same arterial segment is shown in Fig. 3.3. In the case of the pressure wave, backward waves are added to the forward wave and for the flow velocity wave, backward waves are subtracted.

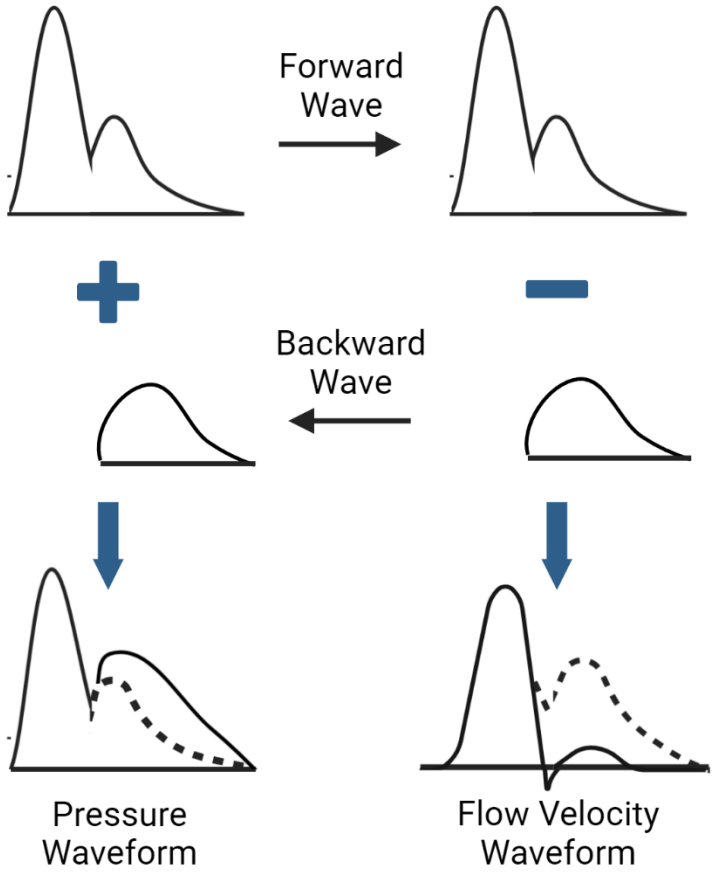

Fig. 3.3. Pressure and velocity waveforms.

Forward and reflected pressure waves in the vascular system are well documented in literature (Li *et al.*, 2017; Westerhof *et al.*, 1972; Alastruey *et al.*, 2014). Wave reflection is an important aspect of diagnosing diseases. As mentioned in Section 1.2.1.1, the disease related to BPH develops with age and the prostatic urethra wall becomes stiffer and get compressed as discussed in Section 3.2.1. This is also the case

in cardiovascular system where the arterial wall gets stiffer with age and during hypertension and in that situation, the extent and speed of reflected waves increase, which is responsible for higher blood pressure. For example, normal blood pressure is less than 120 systolic and 80 diastolic, however, during a hypertensive crisis, it is over 180 systolic and/or higher than 120 diastolic (Governatori & PollackJr., 2018). Li *et al.* (2013) found that the PreWV of blood in the case of standard condition is 6.03 ± 1.68 m/s, but it is 6.69 ± 2.08 m/s in the case of hypertension. The effect of stiffness on wave dynamics was studied by several researchers and it was found that PreWV increases with age (Borlotti *et al.*, 2012; Hirata *et al.*, 2006). In an aging effect analysis, Kroner *et al.* (2014) found that blood flow volume in the internal carotid artery is 177 ± 42 mL/min/m^2 for older (age > 45 years) whereas it is 147 ± 32 mL/min/m^2 for younger (age < 30 years). Vappou *et al.* (2010) studied arterial stiffness effect *in vivo* using pulse wave imaging and found a similar trend. This clearly demonstrates the effect of reflection in pressure wave velocity in fluid flow systems with resistance or impedance.

3.3 Methodology for Imaging Pressure Wave Velocity

The processing methodology for deriving PreWV is described. Fig. 3.4 shows a flowchart to estimate the PreWV using processed RF data of multiple acquisitions obtained from HiFRUS imaging of a flow vessel that has a lumen with an upper and lower wall of tissue.

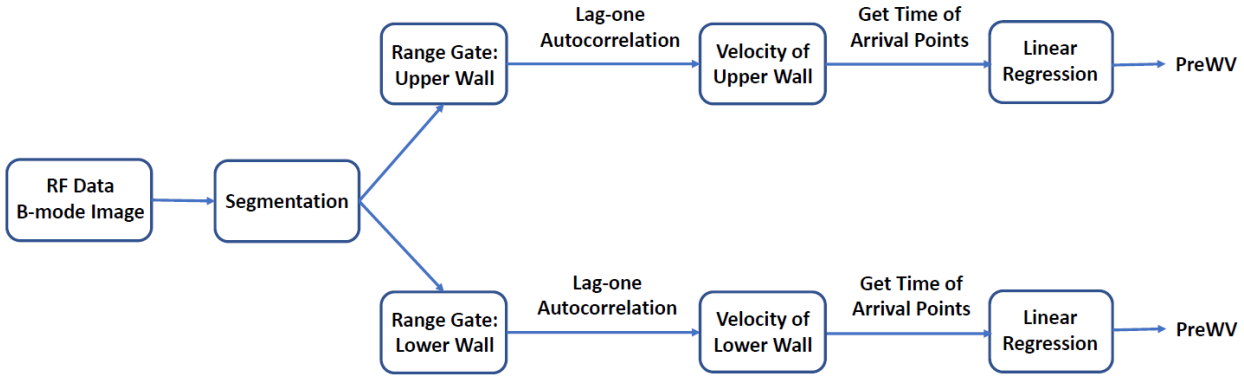

Fig. 3.4. Flowchart for PreWV estimation process.

The derivation of the vessel's wall velocities as regions of interest in the B-mode image is a particular stage of importance in the flow chart. The mean velocity of a moving tissue particle is calculated using Eq. 3-6, which is derived after rearranging and slightly modifying Eq. 2-1 for mean Doppler frequency.

$$\bar{v} = \frac{\bar{f}_D c}{2 f_0 Cos\theta} \tag{3-6}$$

What makes the mean velocity useful in this case is how the mean Doppler frequency is easily calculated to track motion. At a particular lateral position of interest in a M by N pixel image, the magnitude and phase across frames is recorded. This 'slow-time' signal is formed for each lateral view across the image. Doppler frequency is then calculated from the short-time Fourier transform of these signals. To derive the mean Doppler frequency, a single shift sliding window is finally performed on the Doppler processed signals via the lag-one autocorrelation algorithm, which is discussed further in Section 3.3.1.

3.3.1 Tissue Motion Estimation with Lag One Autocorrelation

Derivation of the relationship between the lag-one autocorrelation and the mean Doppler frequency is described. Wiener-Khinchin theorem of signal processing, which relates power spectra to time-domain autocorrelation, can be used to relate the two concepts (Ricker, 2003). To start, the mean frequency can be expressed in terms of the zero-lag autocorrelation function in Eq. 3-7.

$$\bar{f}_D = \frac{\int_{-\infty}^{\infty} f\left(\int_{-\infty}^{\infty} R(\tau)e^{-j2\pi f\tau}d\tau\right)df}{\int_{-\infty}^{\infty}\left(\int_{-\infty}^{\infty} R(\tau)e^{-j2\pi f\tau}d\tau\right)df} = \frac{\int_{-\infty}^{\infty} fP(f)df}{\int_{-\infty}^{\infty} P(f)df} = \frac{\dot{R}(0)}{j2\pi R(0)} \tag{3-7}$$

Where $P(f)$ is the power spectrum, $R(0)$ and $\dot{R}(0)$ is the zero-lag autocorrelation and its first derivative of the time domain signal, $R(\tau)$, respectively. The general analytical form of $R(\tau)$ is expressed as $R(\tau) = A(\tau)e^{j\phi(\tau)}$, where $A(\tau)$ is the amplitude and $\phi(\tau)$ is the phase shift as a function of lag τ. For zero-lag, i.e. $\tau = 0$, $R(0) = A(0)$ with only the squared magnitude of the signal and zero phase, while $\dot{R}(0) = \dot{A}(0) + j\dot{\phi}(0)A(0)$ where $\dot{A}(0) = 0$ as there is no changes in amplitude for zero time-shift. Therefore, $\dot{R}(0) = j\dot{\phi}(0)A(0)$. Thus, the mean frequency is more clearly related to the autocorrelation phase of the signal in Eq. 3-8.

$$\bar{f}_D = \frac{j\dot{\phi}(0)A(0)}{j2\pi A(0)} = \frac{\dot{\phi}(0)}{2\pi} \tag{3-8}$$

In the case of pulsed Doppler, the phase $\dot{\phi}(0)$ can be expressed as a slope in Eq. 3-9 based on the sampling period between each acquisition from the HiFRUS data, i.e. the pulse repetition interval T_{PRI}.

$$\dot{\phi}(0) = \frac{\phi(T_{PRI}) - \phi(0)}{T_{PRI}} = \frac{\phi(T_{PRI})}{T_{PRI}},\ \phi(0) = 0 \tag{3-9}$$

This is significant to simplifying the calculation of tracking motion as the autocorrelation phase at T_{PRI} is only needed to calculate the mean frequency, which Eq. 3-10 shows in the case of one-lag autocorrelation.

$$\phi(T_{PRI}) = \angle R(T_{PRI}) = \angle \left[\sum_{k=1}^{N_D} s_D^*(k;m,n) s_D(k+1;m,n) \right] \tag{3-10}$$

Where N_D is the ensemble size of the sliding window expressed as the number of frames, k is the current frame within the ensemble being evaluated, s_D is the range gate autocorrelated with its conjugate, s_D^*, at the $(m,n)^{\text{th}}$ pixel in a M by N complex format of the image, and f_{PRI} is the reciprocal of pulse repetition interval also known as the pulse repetition frequency. The mean Doppler frequency at the $(m,n)^{\text{th}}$ pixel in a M by N complex image is related to the one-lag autocorrelation phase at T_{PRI} shown in Eq. 3-11.

$$\bar{f}_D(m,n) = f_{PRI} \frac{\phi(T_{PRI})}{2\pi} = \frac{f_{PRI}}{2\pi} \angle \left[\sum_{k=1}^{N_D} s_D^*(k;m,n) s_D(k+1;m,n) \right] \tag{3-11}$$

Thus, the mean velocity at any pixel position(s), or range gate, can be calculated by Eq. 3-12.

$$\bar{v}(m,n) = \frac{c}{2f_0} \bar{f}_D(m,n) \tag{3-12}$$

The PreWV is calculated using this mean velocity with lag one autocorrelation by selecting the range gate area on the urethral phantom walls. Fig. 3.5 below illustrates the pertinent steps in the processing pipeline for PreWV derivation where only the lower wall of a tortuous flow phantom is used as an example.

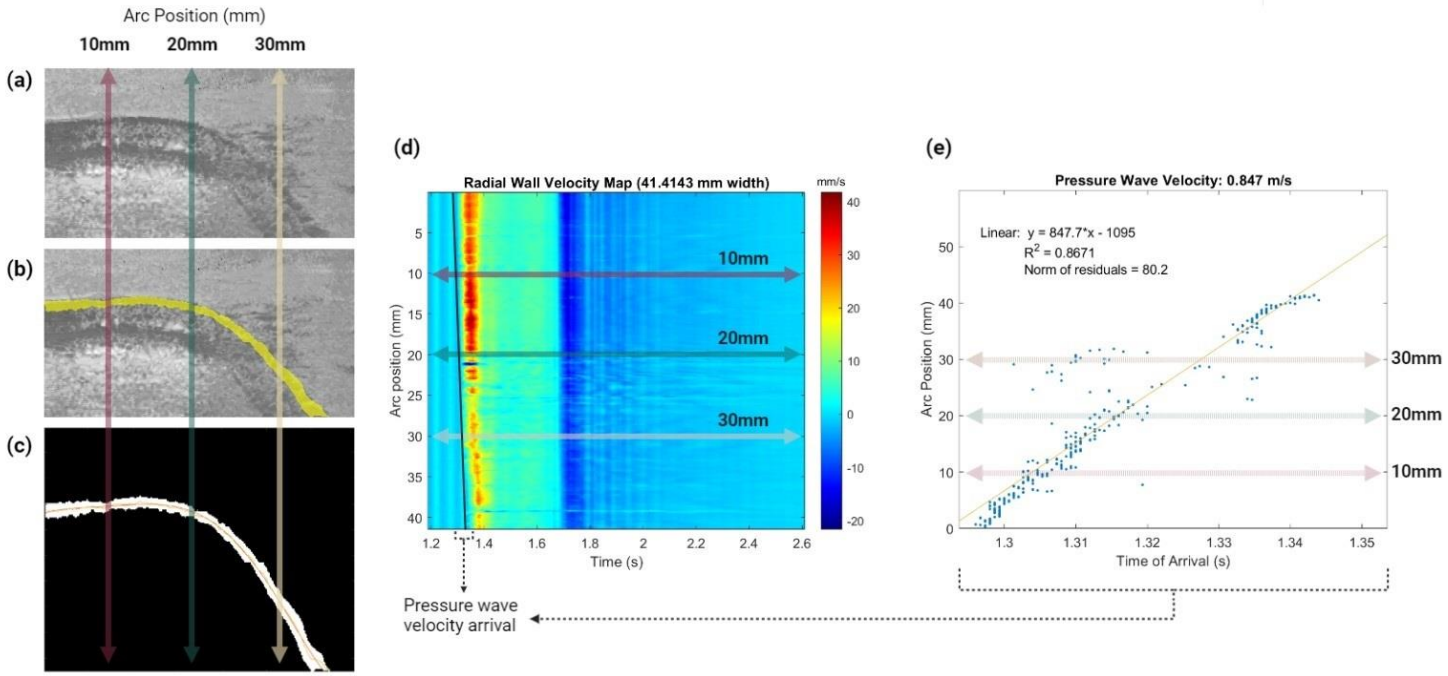

Fig. 3.5. PreWV processing pipeline. a) Tissue doppler frame with max distension is selected for segmentation. b) Image mask is created along the contour of the phantom. c) Polynomial fitting is applied to get the arc position along the contour of the image mask. d) A velocity colormap is derived using lag-1 autocorrelation; the time range for the arrival of the PreWV is determined. e) Linear regression is applied to the arrival sites found at the foot of the pressure wave at each position along the arc.

Some heuristics are applied in determining the PreWV. First, the wall velocity colormap is filtered out based on the range-gate region the segmentation is applied on. For example, for a range gate where the upper wall is segmented, during events such as expansion or contraction and looking along the lateral view of the range-gate, it is expected that the direction of the wall velocity is positive during expansion, and negative during contraction of the upper wall. For lateral positions that have wall velocities that do not match this, they are filtered out. This is applied because the segmentation mask is a static image applied on a slow-time ensemble of moving images, so it may be the case that the lower wall velocities creep into the range-gate when isolating for upper wall only due to this segmenting limitation. The opposite is true when segmenting for the lower wall only. The second heuristic applied is in determining the time of arrival points based on the wall velocity curve at each lateral position of the range gate. Previous literature has described different methods to obtain the beginning time point for pressure wave propagation, however the most common is choosing the foot site that is just before the wall velocity magnitude increases substantially (Pereira *et al.,* 2015; Vappou *et al.*, 2010). This is because it is the most reflection-free zone compared to the half-max, or peak of the wall velocity magnitude curve. In this processing pipeline, the second derivative method is employed where changes in the curve concavity are used to detect the foot site for obtaining the time of arrival point.

3.3.2 Current Flow Phantoms to Assess Performance

Study of the urinary flow dynamics is currently one new research area that is challenging in urology because accurate estimation of fluid flow in urology using ultrasound remains unaddressed by the scientific community. Analyzing the functional impact of pathological features, like urethral obstruction, is important in urethral dynamics. This is due to the challenges of directly executing on a patient, i.e. *in vivo* because of the sensitivity gap in the measure for bladder outlet obstruction. This is a special problem as the construction and orientation of urethra and bladder wall thickness complicate the processing of ultrasound signals. Hence, there are huge opportunities to explore, design, and implement simulated urethra phantoms to detect prostate diseases by estimating the fluid flow in the urinary tract.

Many ultrasound studies involve the use of phantom because this tool provides a cost-effective solution to assess an optimum treatment plan in a low-risk *in-vitro* environment before applying *in-vivo*

clinical trials. The application of tissue-mimicking phantom is especially useful for applying therapeutic ultrasound techniques (Kharine *et al.*, 2003; Pogue & Patterson, 2006; Arora *et al.*, 2005; Kumar *et al.*, 2022; Maxwell *et al.*, 2010). Although there are applications of the phantom in biomedical research for fluid flow study, most of them are related to the cardiovascular system (Chen *et al.*, 2009; Badescu *et al.*, 2018; Nisar *et al.*, 2020; Boice *et al.*, 2022; Corrado *et al.*, 2021). Cao *et al.* (2013) studied elastography on prostate cancer using tissue-mimicking phantom, while other researchers studied designing urethra phantoms with the goal of simulating the geometric, mechanical, and hydrodynamic characteristics of the male prostatic urethra (Ishii *et al.*, 2017; Lai *et al.*, 2013; Yiu & Yu, 2017). A new urodynamic imaging framework termed contrast-enhanced urodynamic vector projectile imaging (CE-UroVPI) provides time-resolved visualization of urinary flow and urethral deformation during the initiation phase of voiding, which was devised with the use of the phantom for experiments (Ishii *et al.*, 2020). A method to investigate the relationship between voiding dysfunction and alteration of the shape of the prostatic urethra by processing endoscopic video footage, and analyzing the fluid dynamics of the urine stream off-site was also documented in the literature (Ishii *et al.*, 2014a).

The orientation of the male urethra in the prostatic area is a curved tubular structure (tortuous) with various angles as shown in Fig. 3.6.

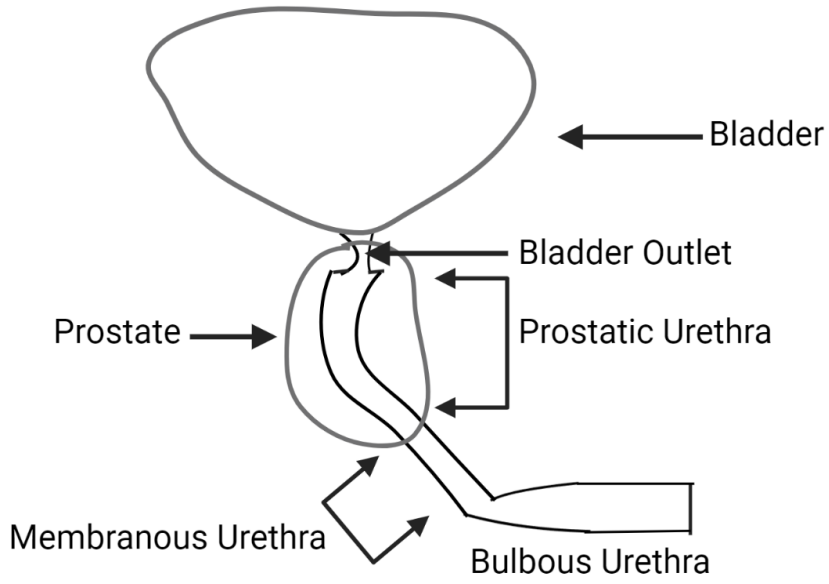

Fig. 3.6. An anatomy of the prostate gland showing a tortuous prostatic urethra.

Ishii *et al.* (2019) developed a novel phantom design protocol that models a realistic urinary tract with its geometric characteristics, and this protocol has been adapted in this thesis research as a basis for developing new phantoms for PreWV urodynamic study *in-vitro*.

3.4 Chapter Summary

This chapter discussed the PreWV, which is a new modality in ultrasound imaging of the male urinary tract having the symptom of BPH. Details on wave dynamics was explained giving examples of forward and reflected waves to explain concepts related to the characteristics of PreWV. How the PreWV characteristics are originated in BPH is detailed in this chapter as well as the methodology to estimate tissue motion using lag one autocorrelation. This chapter also revealed the theory of how the pressure wave increases due to wave reflection caused by impedance from compressed urethra associated with BPH, and by the tortuous geometry of the male urinary tract. Also shown in this chapter is the basic anatomy of the prostatic urethra for designing a phantom study to assess the PreWV performance.

CHAPTER 4: IN-VITRO EXPERIMENTAL SETUP

4.1 Chapter Overview

This chapter describes the experimental setup and data acquisition procedures for the in-vitro tortuous flow phantom platform used to calibrate the performance of the pressure wave urodynamic imaging framework. Section 4.2 shows an overview of the experimental setup and elaborates on the phantom design process, imaging box setup, flow pump parameters for the flow circuit, and HiFRUS data acquisition settings.

4.2 Tortuous Flow Phantom Platform

Fig. 4.1 shows the complete *in-vitro* setup of the tortuous phantom platform.

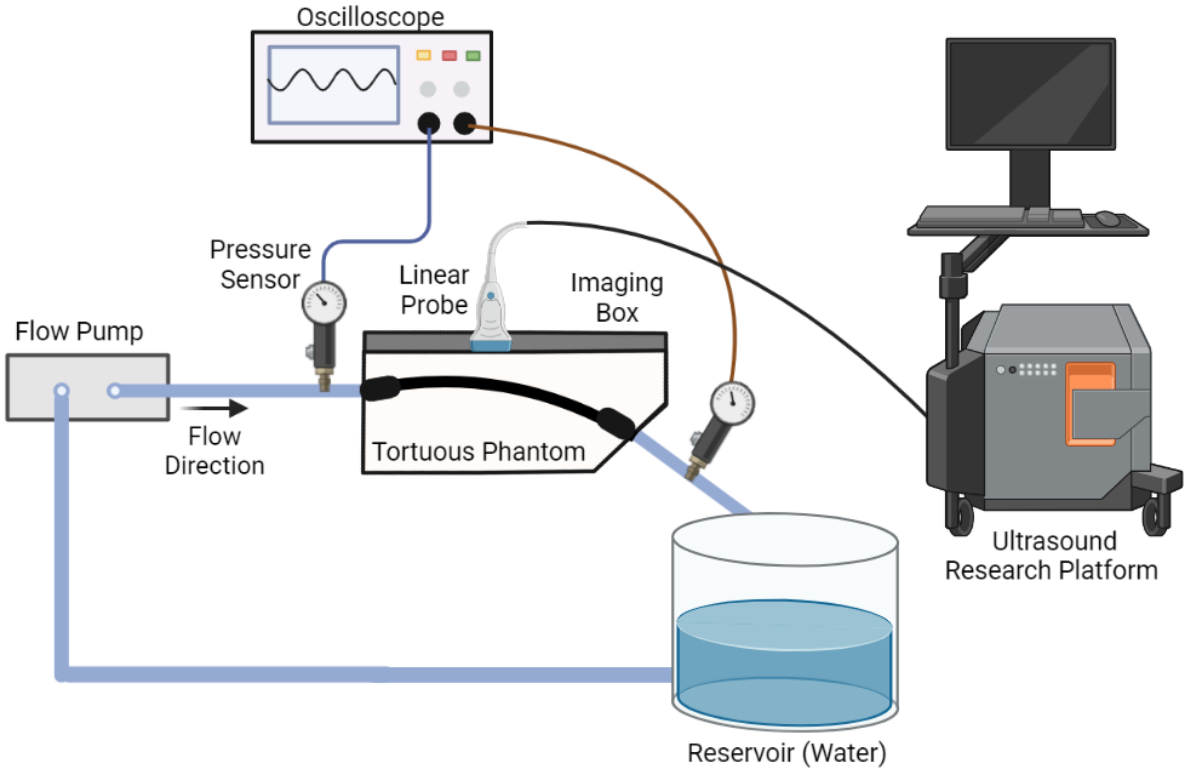

Fig. 4.1. Overview of the tortuous phantom flow circuit experimental setup.

A pump and reservoir are used to circulate water into the phantom, pressure sensors placed at the inlet and outlet of the imaging box are used as reference measurements for the global PreWV, a linear array

transducer connected to the ultrasound research platform is used to collect HiFRUS data of the phantom for pressure wave analysis.

4.2.1 Phantom Design and Fabrication

A new tortuous flow phantom for urodynamic pressure wave imaging studies was designed and fabricated to test the effect of reflections on PreWV occurring before and after the bend region of the phantom. The purpose of this phantom is to isolate the tortuous feature of the male urinary tract for calibration of the pressure wave imaging framework. The phantom parameters are summarized in Table 4.1.

Table 4.1. Key phantom design parameters for *in-vitro* experiments.

Name	Lumen Dimensions	Port Dimensions	Transition Dimensions	Layout (Length)
30° Phantom	Concentric lumen, 6 mm lumen diameter, 3 mm wall thickness	6 mm diameter, 7 mm wall thickness	6 mm diameter, 2 mm change in wall thickness per 1 cm length	Inlet port (3 cm), Transition (2 cm), Before bend (10 cm), Bend region (2 cm), After bend (10 cm), Transition (2 cm), Outlet port (3 cm)
45° Phantom				

In designing the phantom to study the effects of the PreWV response from the tortuous geometry of the urinary tract, three main constraints are considered: The degree of curvature, wall thickness, and the length of the lumen. To assess the impact of tortuosity only, a reference angle of 30º and a wall thickness of 3 mm with a concentric lumen of 6 mm in diameter were selected. This is based on what previous works have described for the anatomic dimensions of a normal male urinary tract (McNeal, 1981; Humphrey, 2014; Ishii *et al.*, 2014b; Tojo *et al.*, 1994). Another similar phantom with a 15º increase in curvature was designed with the goal of assessing the significance in the variability of the degree of curvature on the PreWV. Finally, the length of both phantoms was kept at 260 mm overall to mitigate the impact of reflections at the inlet and outlet ports of the imaging box. With these parameters, the phantom mold was prepared using SolidWorks (Dassault Systèmes, Waltham, MA, USA), which is a computer-aided design (CAD) software, to be later three-dimensionally (3D) printed (Model DX; Creatbot 3-D Printer, Zhengzhou, China) prior to casting the actual phantom. Fig. 4.2 illustrates the phantom design parameters. Note that the inlet and outlet ports of the phantom have an increased wall tissue thickness of 7 mm to prevent the phantom

from tearing when mounting at the ports since a 3 mm wall thickness was too thin and fragile to use for the ports.

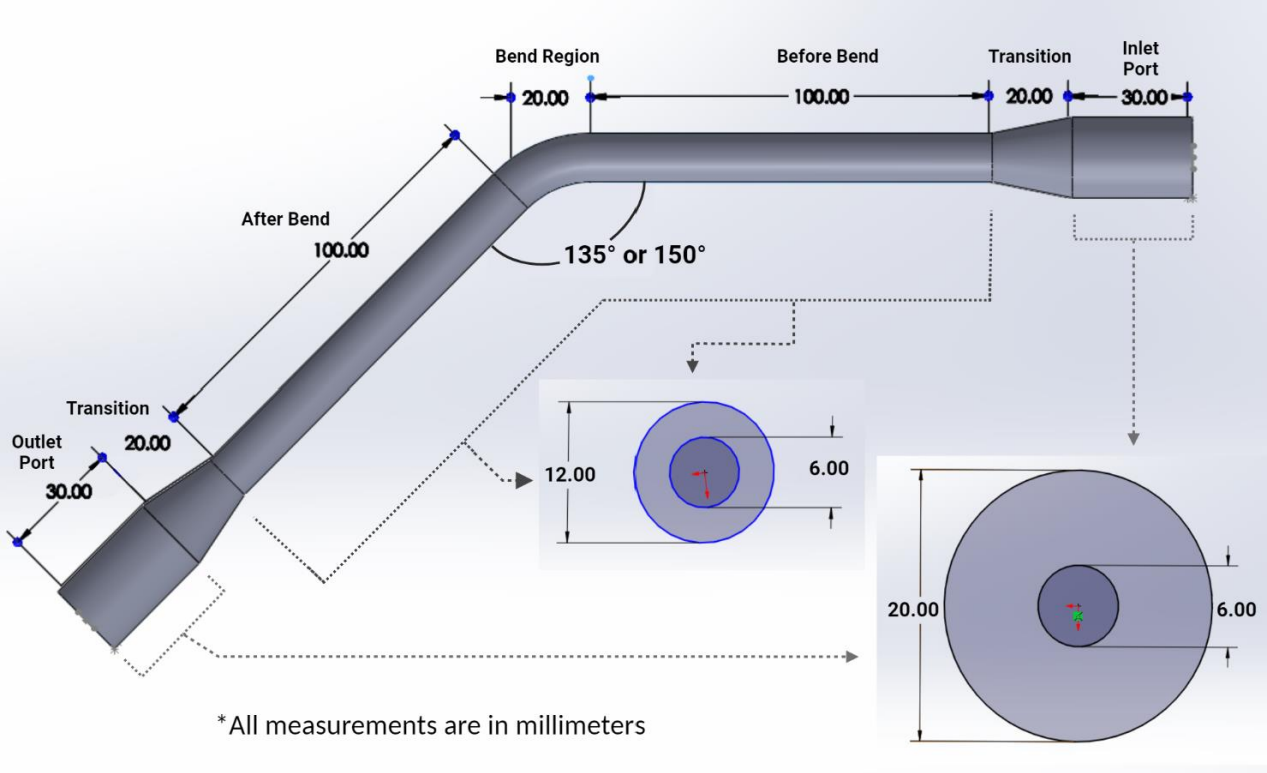

Fig. 4.2. Phantom CAD models. Both 30° and 45° phantoms shared the same features except for the angle of bend.

The methodology in the phantom mold design is based on a modified lost-core protocol described in previous works (Ishii *et al.*, 2019). The original protocol involves fabricating the phantom in a 3D printed outer mold with the negative 3D printed version of the lumen, known as the inner core, to pull out later in the fabrication process. The outer mold has two halves with a negative replica of the geometry of the phantom and the inner core support structure. It also features inlet and outlet ducts for injection of urethra tissue mimicking material during the fabrication step. The modification to this protocol builds on a solid core support structure attached to the ends of the inner core in SolidWorks. This was done to address problems with the core sagging and to improve uniformity of the posterior and anterior walls in the fabricated phantom. To minimize dimensional variations in the printed product, the inner core was designed in SolidWorks to be upright with a basic supporting structure. Fig. 4.3 shows the CAD models of the 30º and 45º phantom molds along with the core design. The 3D printed models were constructed with polylactic acid thermoplastic (PLA) material. These models served as the basis for the fabrication step in casting the

actual phantom. In attempts to reliably produce phantoms with, an epoxy-based version of the PLA outer mold was decided against due to process variations that made it difficult to preserve the dimensions of the original mold when working with epoxy.

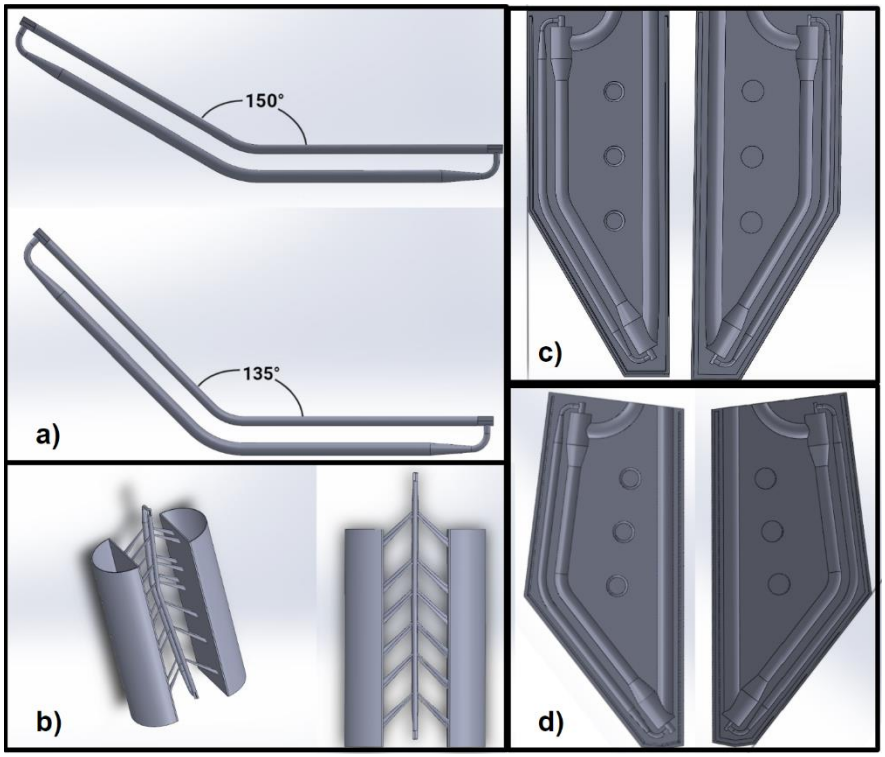

Fig. 4.3. Overview of the assembly materials used to cast the phantoms. a) The inner cores used to produce the phantom lumen; both cores feature a support to prevent sagging. b) Support structure to print the cores upright, these were removed once the print completed. c) 30° phantom outer mold halves. d) 45° phantom outer mold halves.

To cast the tortuous phantom, a mixture was prepared according to a previous protocol for fabricating urethral mimicking tissue (Ishii *et al.*, 2019). This was a polyvinyl alcohol (PVA) solution where the composition is described in Table 4.2.

Table 4.2. The solution composition for making the tortuous phantom.

Material	Percentage (by weight)	Part number and Manufacturer
Distilled water	90.7%	N/A
Polyvinyl alcohol (PVA)	8%	341584; Sigma-Aldrich
Fine graphite powder	1%	282863; Sigma-Aldrich
Potassium sorbate	0.3%	85520; Sigma-Aldrich

The PVA can form into a hydrogel with a useful property that allows the elastic modulus of the solution it is in to be controlled via repeated cycles of freezing and thawing to establish crosslinks, while being ultrasound compatible (Lai *et al.*, 2013). The graphite serves as a scattering medium for ultrasound, and the potassium sorbate is used as a preservative. Based on the previously established protocol, the solution was mixed for 40 minutes at 90ºC and cooled for 24 hours (Lai *et al.*, 2013).

Once the solution has cooled, the phantom is ready to be casted. In the casting step, the printed inner core is slightly lubricated, which assists in the removal of the core from the phantom later in the process and placed into the outer mold. The two halves of the outer mold are then closed together with duct tape applied around the edges and secured with clamps. The PVA solution is injected into the inlet of the outer mold, while the outlet allows for overflow of solution as the mixture fills up the volume of the phantom. The entire assembly is then placed into the freezer where the casted phantom undergoes a freeze-thaw cycle process and solidifies. This process also facilitates cross-linking where the phantom is frozen for 24 hours at -20ºC in the freezer and then thawed for another 24 hours at 5ºC in the refrigerator, which is known as one freeze-thaw cycle. After two freeze-thaw cycles the phantom mimics elastic properties of urethral tissue, yielding a young's modulus of 26.6 ± 4.0 kPa from uniaxial tensile testing that is consistent with what has been previously reported in literature (Ishii *et al.*, 2019; Natali et al., 2016). Furthermore, the acoustic speed and attenuation coefficient of a PVA based tissue mimic were previously found to be 1535 m/s and 0.229 dB/(cm•MHz) respectively (Chee *et al.*, 2016). Finally, the mold housing is removed, and the inner core support is snapped off so that the core can be carefully pulled out to complete the process. Fig. 4.4 shows the fabricated 30º and 45º bent phantoms. The phantoms were preserved in water to avoid dehydration of the PVA based urethral tissue mimic before setting up the imaging box.

Fig. 4.4. The tortuous phantoms casted after two freeze-thaw cycles. Top: 30° phantom. Bottom: 45° phantom.

4.2.2 Imaging Box Setup

The flow phantoms prepared were next fitted in a 3D printed imaging box to encase it in prostatic tissue mimic slab. The CAD model of the box is shown in Fig. 4.5. The inner dimensions of the 30º phantom imaging box were 304 x 80 x 105 mm^3 (length x width x height), while the 45º phantom imaging box had inner dimensions of 290 x 80 x 120 mm^3. Both boxes feature a 17.3 mm diameter hole cut-out at opposite ends that function as ports to allow flow to enter and leave. An inlet and outlet quick-fit flow connector (EW-06361-61; Cole-Parmer, Vernon Hills, IL, USA) were installed on the ports of the box where the phantom inlet and outlet are secured to. Both imaging boxes include an angled wall within the inner volume of the box to accommodate a cover. The purpose of this cover is to limit the amount of volume the prostatic tissue mimic material would be needed to encase the phantom in, and to maintain a consistent 1 cm depth between the ultrasound probe to the phantom surface for the entire length of the phantom.

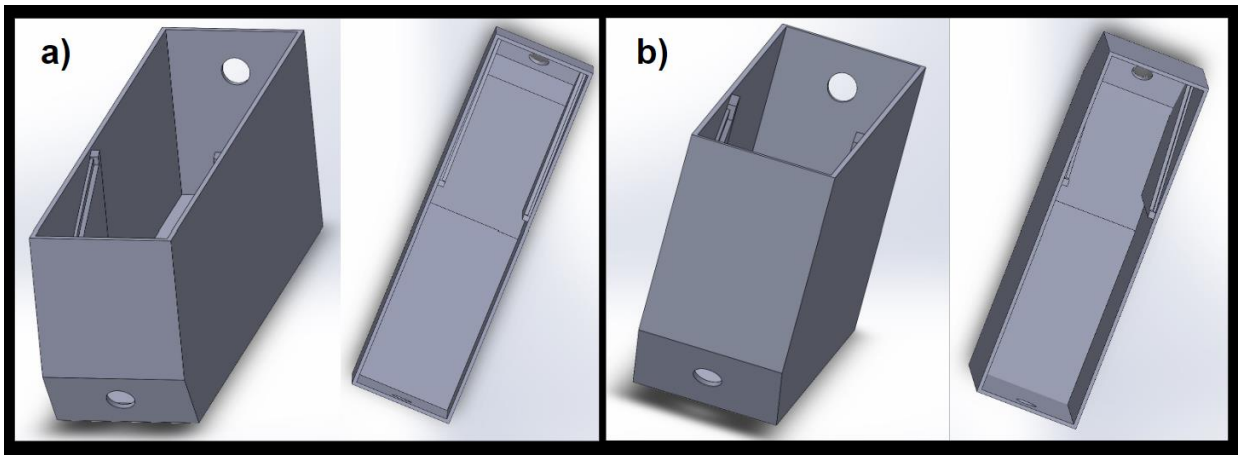

Fig 4.5. Phantom box design with support for inner slanted cover. a) 30º phantom imaging box. b) 45º phantom imaging box.

After the tortuous phantom is mounted inside the imaging box, but before encasing it in prostatic tissue mimic, five steps were taken to extract air present in the lumen and produce a collapsed state. First the inlet and outlet of the phantom were tightened at the ports with zip ties. Second, the box was filled with water to provide buoyant support for voiding air out of the phantom in later steps. Third, 2-way stopcock flow tubes with a 20-cc syringe attached on one end were secured to both outer ports of the imaging box, and air within the lumen of the phantom was slowly suctioned out using the syringes. While air was being suctioned out, external pressure was applied onto the phantom lumen by pressing along the circumference of the phantom surface and pinching the air in the lumen out towards the syringe. This step was repeated two times, once towards the inlet syringe and again towards the outlet syringe. Fourth, a small clamp was attached at the bend portion of the phantom to further prevent any air pockets forming within the bend portion of the phantom, and then air was suctioned out of the phantom at the outlet and again at the inlet using the syringe. Finally, the clamp was removed. Once the phantom lumen was void of air and collapsed, the water in the imaging box was discarded, the stopcock at the inlet and outlet were engaged to block any airflow into the tubes, and the syringes were detached from the closed off tubes. The bend portion of the phantom was kept level by wrapping a piece of tungsten wire underneath the position of the bend and gluing the ends of the wire onto the outer walls of the imaging box to keep it suspended. The purpose of this was to prevent the phantom from sagging when applying the prostatic tissue mimic and maintain the angle of bend of the phantom. Next, the prostatic tissue mimic was casted.

The prostatic tissue mimic was fabricated according to a similar previous protocol (Ishii *et al.*, 2019). This slab was based on an agar-gelatin mixture where the composition is described in Table 4.3.

Table 4.3. The slab composition for fabricating the prostatic tissue mimic.

Material	Percentage (by weight)	Part number and Manufacturer
Distilled water	93.7%	N/A
Agar	1.0%	A1296; Sigma-Aldrich
Gelatin	5.0%	G2500; Sigma-Aldrich
Potassium sorbate	0.3%	85520; Sigma-Aldrich

The mixture was first dissolved in a beaker of distilled water at 90ºC and stirred constantly for 20 minutes. Then it was cooled down to 45ºC while continuing to be mixed constantly. The constant mixing prevented the solution from solidifying into non-uniform layers while cooling down. It was found that keeping the temperature at 45ºC for the larger volume of agar-gelatin needed to fill the imaging box was warm enough such that the solution would not solidify too quickly when transferring the contents of the beaker into the box. Meanwhile, the cover for the imaging box was seated and taped onto edges of the angled walls found on the sides of the inner volume of the box. A small pouch of water in a plastic bag was placed on top of the cover to apply enough pressure such that no solution would leak out of the cover's edges. Once the agar-gelatin solution was at the desired temperature, it was transferred into the imaging box and then the box was left to solidify in the refrigerator for 12 hours at 5ºC. Previous literature measured the acoustic speed of an agar-gelatin based slab as 1510 m/s and its attenuation coefficient as 0.145 dB/(cm•MHz) (Chee *et al.*, 2016). Finally, the imaging box setup with the casted prostatic tissue mimic slab was removed from the refrigerator, and the plastic pouch, the cover, and the tungsten wire were also carefully removed. Fig. 4.6 shows the imaging box with the collapsed phantom encased in the prostatic tissue mimic slab.

Fig. 4.6. Imaging box with slanted cover removed showing prostatic tissue mimic slab casted over the collapsed phantom.

4.2.3 Flow Pump Parameters

The flow circuit test bench consisted of the imaging box, a reservoir filled with 1800 mL of water, and a programmable flow pump that was designed inhouse; these components were connected via flow tubes (Ho *et al.*, 2017). The imaging box was setup 850 mm above the reservoir and was at the same height level with the flow pump such that there was no pressure differential from the outlet of the flow pump to the inlet of the imaging box. The reservoir filled with water is used as a buffer and positioned below the outlet of the imaging box to maintain a pressure difference downstream and lets the phantom return to its collapsed state at the end of every flow cycle. To mimic a practical voiding episode of the disease model, the flow pump was programmed to output at 7 mL/s constant flow rate based on previous literature with a period of 4 seconds and 15% duty cycle (Ishii *et al.*, 2019). Thus, the on-time for constant flow was 0.6 seconds and the off-time was 3.4 seconds. A short duration of flow is needed to only simulate the initiation phase where the bladder outlet opens during a practical voiding episode as that is the moment where pressure wave propagation begins. The particular off-time is needed to allow the phantom under test to return back to its resting collapsed state, which is similar to the urethra in the termination phase of a voiding episode (Ishii *et al.*, 2019). Next the data acquisition procedure is described.

4.3 Data Acquisition

Two methods of measurements were made to acquire data for PreWV experiments on the tortuous flow phantom platform: 1) HiFRUS, and 2) Pressure sensors.

4.3.1 High-frame-rate Ultrasound Data Acquisition

For HiFRUS acquisitions, steered plane-wave transmissions were made in regions of the tortuous phantom for later obtaining the PreWV of those respective regions. This is broken down into three main regions of the phantom: 1) Inlet, 2) Bend, and 3) Outlet. All acquisitions were made on the longitudinal axis of the phantom. 11 samples of each region were acquired using an ultrasound open-research platform (US4US; Warsaw, Poland). Table 4.4 summarizes the HiFRUS acquisition parameters used for phantom experiments. It was found experimentally that transmission angles of -15º and 15º provided a wide enough region of interest for imaging at the bend while the transmission angles of -1º and 1º provided acceptable signal to noise ratio for imaging at the inlet and outlet regions of the phantom.

Table 4.4. Plane-wave imaging parameters for acquiring with us4us.

Parameter	Value
Imaging Probe Type (# of channels)	Linear Array (192 channels)
Imaging Frequency	5 MHz
Pulse Repetition Frequency	6 kHz
Sampling Frequency	25 MHz
Transmit Angles	-15º, -1º, 1º, 15º
Effective Pulse Repetition Frequency	1.5 kHz
Acquisition Duration	4.2 seconds

Isopropyl alcohol was applied onto the surface of the prostatic tissue mimic in the phantom imaging box to fill the air gap between the ultrasound probe head and the prostatic tissue mimic slab surface. The inlet region was imaged starting 5 cm from the inlet port of the phantom imaging box, the bend region was

imaged directly on top of the bend portion of the phantom, which was previously mentioned to be 2 cm in length, and the outlet region was imaged starting 5 cm from the outlet port of the imaging box. Fig. 4.7 illustrates the imaging acquisition areas on the phantom under test.

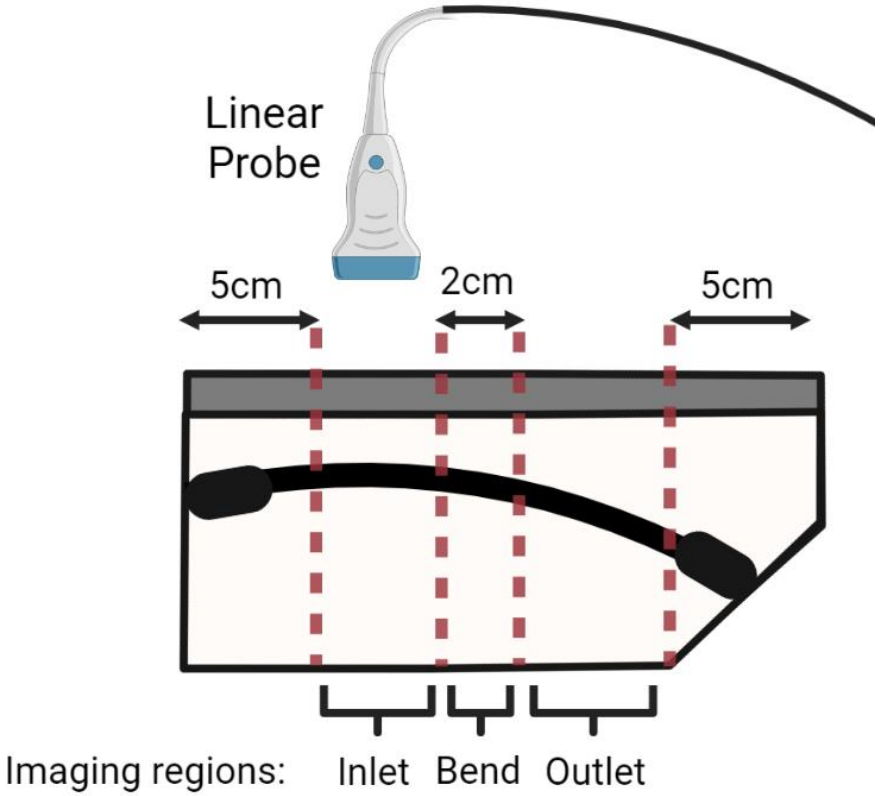

Fig. 4.7. Phantom imaging acquisition areas. 11 samples were acquired at each position.

4.3.2 Pressure Sensor Data Acquisition

For pressure sensors, acquisitions were made to obtain the global and regional PreWV. The global PreWV data was acquired by connecting two pressure sensors at the inlet and outlet ports of the imaging box. The outlet and inlet pressure sensor data are collected and compared on an oscilloscope as voltage waveforms, and the time difference between the two curves are used to determine the transit time. Coupled with the length of the phantom, it is possible to find the global PreWV based on distance divided by transit time.

4.4 Chapter Summary

Due to the fragility of handling PVA phantoms with a low concentration of less than 10% and the time-consuming phantom preparation process that produced varying yields, it was possible to evaluate two

different phantoms for calibration of the pressure wave urodynamic imaging framework. For ground truth values, 11 samples from the pressure sensors were collected at the inlet and outlet ports respectively to match the number of sampled acquisitions using the ultrasound research platform. Overall, the tortuous and collapsed states of the male urinary tract were tested for PreWV validation in this platform using practical voiding flow parameters for diseased BPH patients. While testing for higher voiding flow parameters comparable to urinary flow in healthy males were considered, it was decided against as it was difficult to keep the phantoms intact for a prolonged period when stress testing it with increased flow rates.

CHAPTER 5: EXPERIMENTAL RESULTS

5.1 Chapter Overview

The results of the PreWV for the 30º and 45º phantoms are described in this chapter. The inlet and outlet PreWV from HiFRUS are compared to the global PreWV obtained from the pressure sensors for validation. Then, the subregional PreWV segments at the bend site for each phantom are introduced and the related results are discussed. Finally, statistical significance on the effect of the bend angle on the PreWV response are explored.

5.2 Global Pressure Wave Velocity Validation

With the PreWV derived from the pressure sensors acting as ground truth, the average global PreWV for the 30º phantom was found to be at 0.799 ± 0.0039 m/s (N=11) while the average ultrasound PreWV of the inlet and outlet was measured to be 0.779 ± 0.017 m/s (N=11). No difference of statistical significance was present between the ultrasound and pressure sensor based PreWV for the 30º phantom ($p > 0.14$).

For the 45º phantom, the average global PreWV from the pressure sensors measured to be 0.638 ± 0.033 m/s (N=11), while the average ultrasound PreWV of the inlet and outlet was 0.654 ± 0.023 m/s (N=11). Once again, no difference of statistical significance was present between the ultrasound and the pressure sensor based global PreWV ($p > 0.14$). Thus, the performance of the HiFRUS derived PreWV using the processing methodology described in Section 3.3 from Chapter 3 is valid with regards to obtaining the global PreWV.

5.3 Bend Subregional Pressure Wave Velocity

As it is hypothesized that HiFRUS, with its sub-ms temporal resolution, can accurately resolve PreWV such that it can replace the ground truth for measuring PreWV, it serves to be proven whether the null hypothesis of this is rejected or not. The null hypothesis is that HiFRUS cannot reliably measure PreWV. The following results show statistical significance in the measurement of HiFRUS acquired PreWV for tortuous geometry phantoms that aligns with current theories discussed in Chapter 3. In other words, to test the null hypothesis for non-global PreWV, which is more interesting, an analysis on the statistical significance of the HiFRUS obtained PreWV values at the bend region of the phantom is explored in this section. Specifically, this analysis answers whether the established literature in pressure wave propagation theory for human tissue agrees with the data obtained here. To facilitate this analysis, in

addition to the acquired bend regional PreWV of the 30º and 45º phantoms, the bend regions are also broken down into three subregions for further PreWV analysis: 1) Before the bend, 2) At the bend, and 3) After the bend.

Figs. 5.1 and 5.2 show the box plot comparing the subregional PreWV values before the bend, at the bend, and after the bend for the 30º and 45º phantoms respectively (N=11 for each category in each phantom). No increase in PreWV were found after the bend, rather the opposite was true for both cases ($p < 0.001$). Compared to before the bend, there was a decrease of 0.356 ± 0.17 m/s or a 44% reduction in all observed subregional PreWV after the bend for the 30º phantom, and a decrease of 0.409 ± 0.14 m/s or a 58% reduction in all observed subregional PreWV after the bend for the 45º phantom.

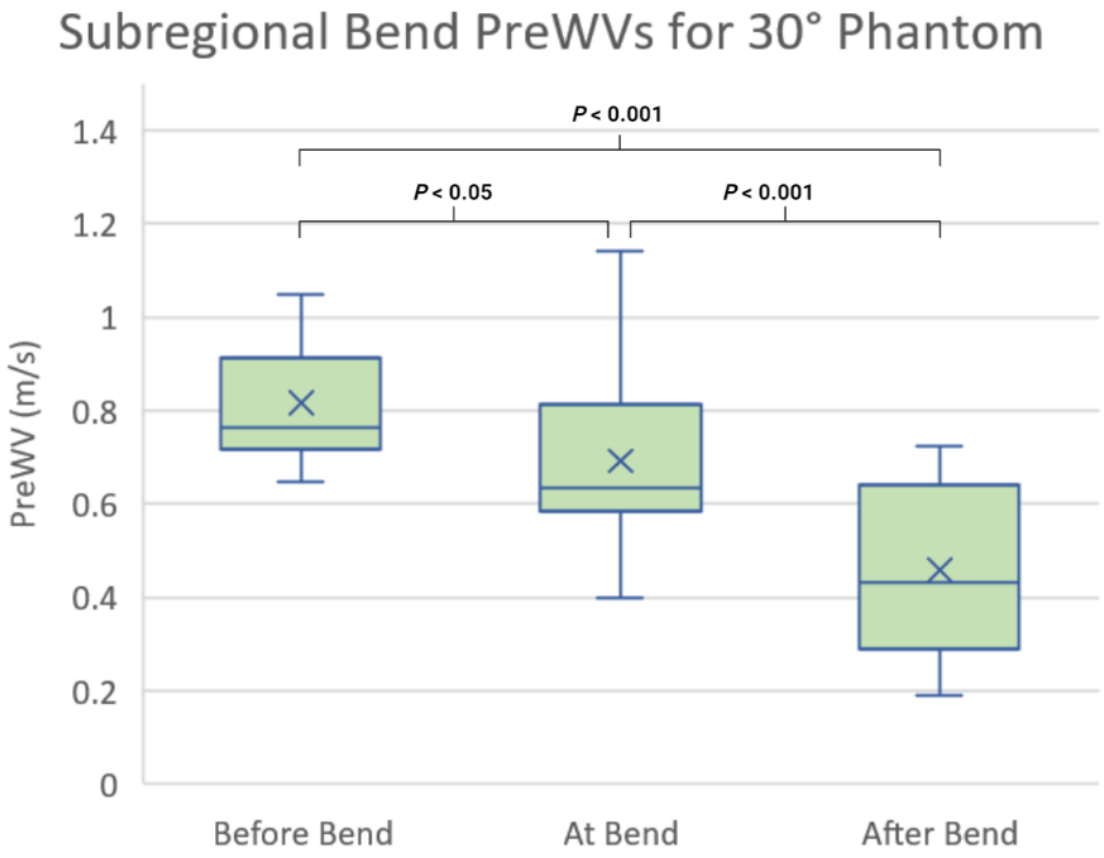

Fig. 5.1. Box and whisker plot comparing the PreWV values before the bend, at the bend, and after the bend subregions for the 30º phantom (N=11 in each category).

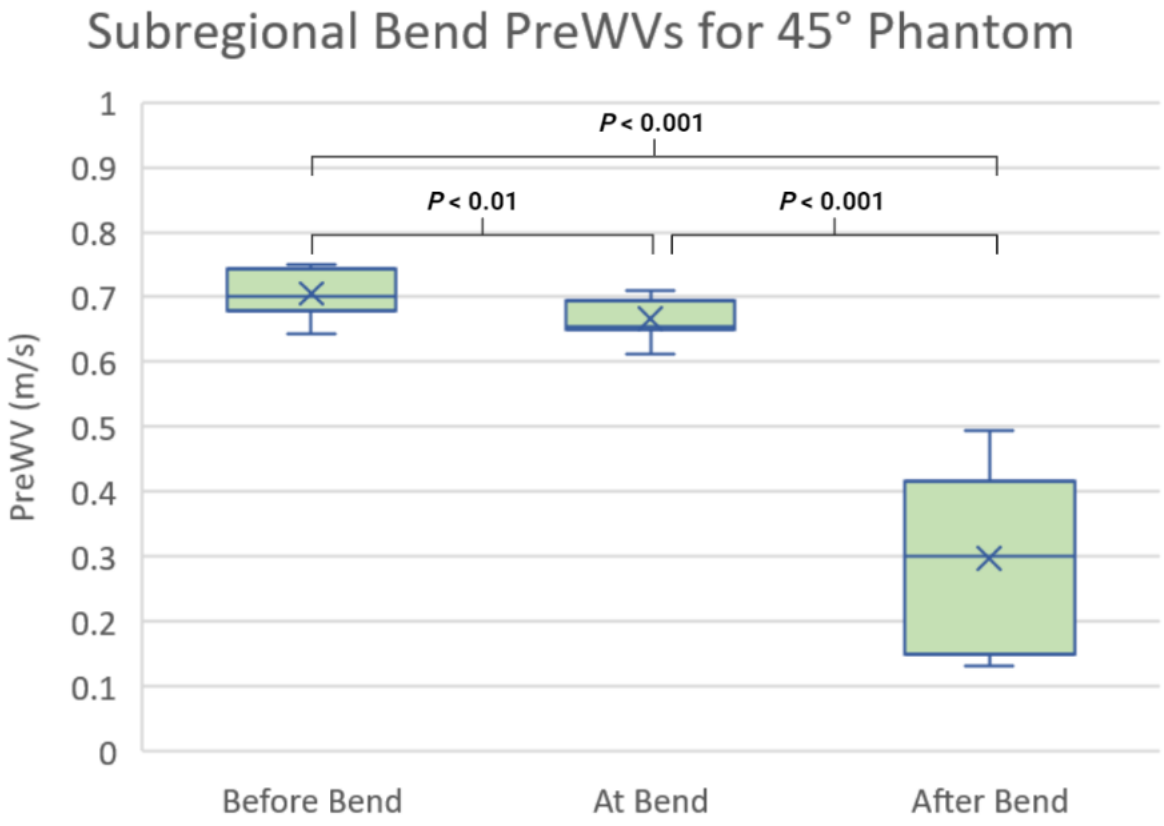

Fig. 5.2. Box and whisker plot comparing the PreWV values before the bend, at the bend, and after the bend subregions for the 45º phantom (N=11 in each category).

Thus, there is statistical difference between PreWV before and after the bend since a notable decrease in PreWV is observed after the bend in both phantoms.

5.4 Effect of the Bend Angle on the Pressure Wave Velocity

Further to this, a box plot comparison between the regional PreWV of the bend region in both phantoms is shown in Fig. 5.3. On first notice, there is indeed a difference between the 30º and 45º bend regional PreWVs ($p < 0.001$), however it is important to highlight that the 30º bend regional PreWVs have a higher variance. This is due to issues in maintaining a good signal to noise ratio during plane-wave acquisitions at the bend region for this phantom.

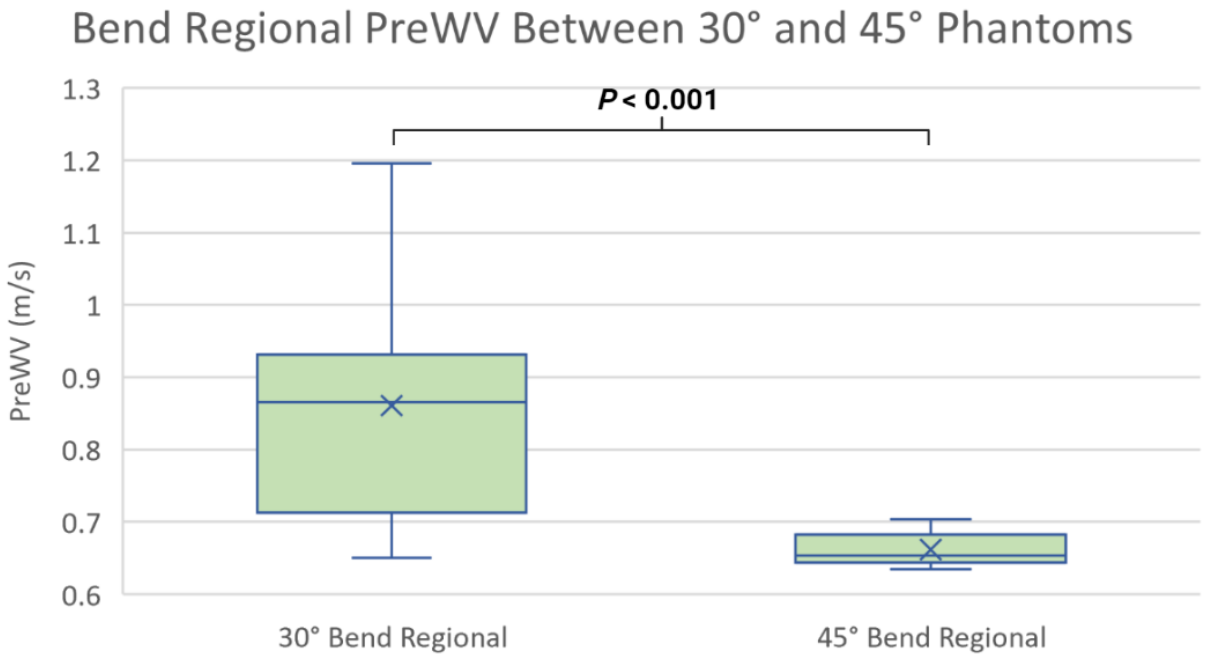

Fig. 5.3. Box and whisker plot comparing overall bend regional PreWV between the 30º and 45º phantoms (N=11).

Furthermore, it was found that as the angle of bend increases, the difference between PreWV before and after the bend increases considerably. As shown from the slope of the regression lines in the Bland-Altman plots in Figs. 5.4 and 5.5 for the 30º and 45º phantoms respectively, for every average PreWV increase, the difference in PreWV before and after the bend are approximately 0.5 times that for the 30º phantom and 2 times that for the 45º phantom. Thus, for a 15º increase in the angle of bend, there is an estimated 4 times increase in the difference between the PreWV before and after the bend, where the PreWV before the bend is on average greater than after the bend. This aligns well with the reflection wave theory explained in Chapter 3 where increases in the overall pressure wave before traversing through a reflection site occur due to an impedance mismatch in the medium of travel. This causes a compounding of the forward pressure wave with the reflected wave near the reflection site, which increases the overall velocity of the pressure wave before decreasing again after the reflection site has been traversed.

Fig. 5.4. Bland-Altman plot for 30° phantom showing the change in the difference between PreWV values before and after the bend as the mean PreWV of the bend region increases.

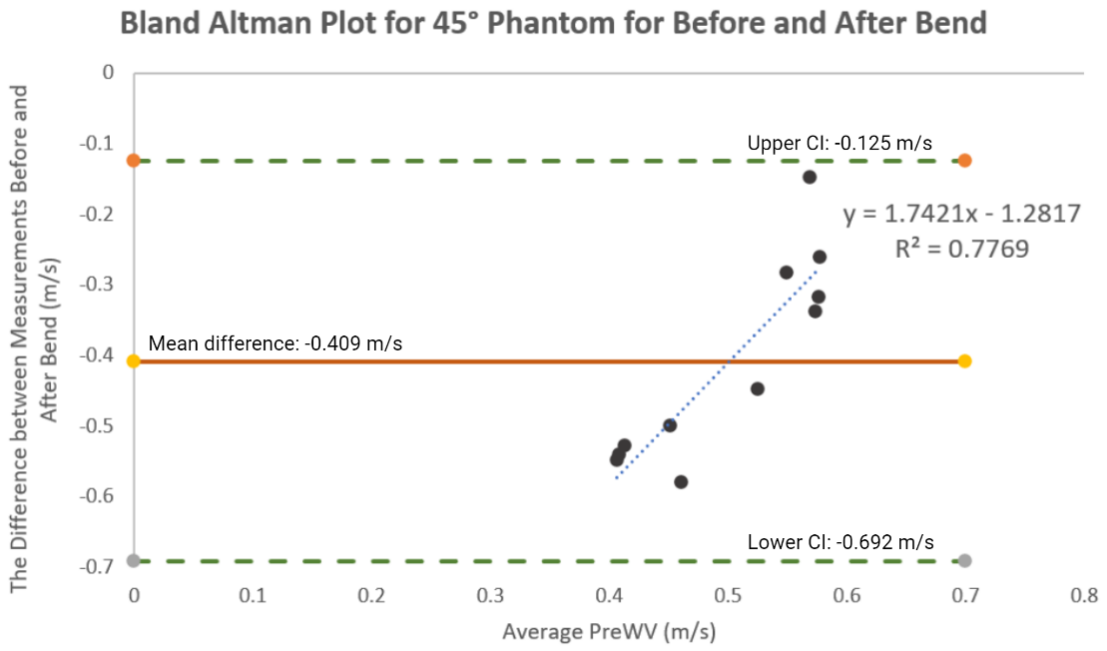

Fig. 5.5. Bland-Altman plot for 45° phantom showing the change in the difference between PreWV values before and after the bend as the mean PreWV of the bend region increases.

5.5 Chapter Summary

The global PreWV response measured using HiFRUS were validated with the pressure sensor data. Furthermore, results of the subregional PreWVs at the bend site conformed to existing knowledge on pressure wave propagation in human tissues. This is significant to validating HiFRUS as an imaging modality that is capable of elucidating subregional pressure wave events within the male urinary tract and could be useful for specific monitoring and diagnosis of BPH compared to the gold standard. Interestingly, the 30° phantom bend PreWV exhibited higher regional PreWV compared to the 45° phantom. This can be due to low measurement signal-to-noise ratio during HiFRUS data acquisition of this phantom as there is a higher variance in the 30° bend regional PreWV. Indeed, this presents a limitation on plane-wave based ultrasound acquisitions as such a transmission type suffers from a decreased region of focus compared to conventional focused beam ultrasound.

CHAPTER 6: SIGNIFICANCE AND IMPACT OF STUDY FINDINGS

6.1 Summary of Contributions

This thesis research addressed the phantom modelling of the urinary tract anatomy for PreWV validation in an *in-vitro* urodynamic study. PreWV is a new measurement type based on ultrasound imaging that is meant for eventual *in-vivo* urodynamic study of patients experiencing disease related to BPH. The main contributions to this research include, but not limited to, the following:

1. Novel tissue mimicking tortuous phantoms modelling features of the human prostatic urethra that can be freely designed and reproduced. Furthermore, they can be used to study *in-vitro* the effects of the bent geometry of the collapsed male urethra on the PreWV using HiFRUS plane wave imaging for calibration experiments.
2. An experimental urodynamic imaging set-up with a reproducible protocol for producing a collapsed state in the phantom, and a unique imaging box design that can allow for *in-vitro* imaging experiments of tortuous geometry phantoms casted in a tissue mimic slab.
3. A ground truth setup to validate the global PreWV obtained from HiFRUS as well as a PreWV processing pipeline that has been validated in this study.
4. The statistical significance on the effect of bend angles of the tortuous phantoms on the PreWV, highlighting the need to calibrate mapping of the PreWV for distinguishing healthy and diseased patients *in-vivo*.

Research findings showed that for both tortuous and collapsible phantoms, the PreWV before the bend is higher than after the bend. This is attributed to the superimposing of backward waves before the bend site that originates from reflections at the bend site, which accounts for a larger PreWV response similar to what was explained in Section 3.2.2 (Fig. 3.3). The agreement of these results with the ground truth and existing pressure wave propagation theory conclusively validates the concept of applying PreWV using HiFRUS for urodynamic imaging studies, which is the novelty of this thesis research.

6.2 Limitations

There are several limitations mentioned in this study that could be addressed. First, the effect of the reflections proved to have a significant impact on the PreWV based on the results of the tortuous flow phantom platform experiments. To address the concern of reflections affecting PreWV results when assessing for BPH models *in-vitro*, it is advised to implement a wave separation method to remove the bias

of the reflected wave. This can also help *in-vivo* to distinguish PreWV between a healthy and a diseased patient by separating PreWV changes from wave reflections and the urethral constriction that is associated with BPH.

Furthermore, it is advised to use synthetic aperture imaging over plane-wave imaging for HiFRUS acquisitions since synthetic aperture imaging provides a wider field of view for focus compared to plane-wave imaging as discussed in Chapter 2 (Fig. 2.4). When compounding the low-resolution images in plane-wave imaging, the field of view focus is narrowed to the region where all the plane waves intersect, thereby restricting the high-resolution image focus that narrows as the depth increases. This decreases the signal-to-noise ratio for regions outside this field, which affected experimental results in this study when examining the bend region of the tortuous phantom. Synthetic aperture imaging would also be appropriate for clinical adoption where transrectal imaging of the prostatic urethra can be employed with a curvilinear field of view that plane-wave imaging cannot support.

Lastly, the most important limitation of this study is that not all variables of a diseased BPH male urinary tract could be modelled and explored separately. It would be next worth modelling the eccentricity of the urethral lumen structure, which is found in the stiff state resulting from urethral obstruction, as a separate phantom for further PreWV validation studies of the HiFRUS based urodynamic imaging framework.

6.3 Future Directions

The overall goal of this research is to non-invasively visualize and quantify urological dynamics at a fine temporal resolution by using a new high-frame-rate ultrasound imaging framework. This thesis research involved the foundational work on the application of a new metric called PreWV that could be used to non-invasively measure and distinguish urethral stiffness while monitoring urinary flow dynamics in male patients suffering from BPH. To cross-validate this concept the following works are recommended in future research:

1) *Development of a HiFRUS-based vector flow imaging scheme for the transrectal probe to measure urinary flow dynamics*

Previous research in urology has demonstrated *in-vitro* that HiFRUS vector flow imaging can be used to show an indication of BPH by visualizing turbulent urinary flow that is characteristic of a diseased male urethra (Ishii *et al.*, 2017 & 2020). Vector flow imaging could be positioned to identify early factors of BPH, but these studies were conducted using linear probes, whereas clinicians use transrectal probes for

the increased field of view they provide in visualizing the entire lower urinary tract (LUT) compared to linear probes (Lee & Roh, 2017; Angelsen *et al.*, 1995; Galosi *et al*., 2012; Pate *et al.*, 2020; Rathaus *et al*., 1991). However, real-time vector flow imaging at high frame rates with the transrectal probe has yet to be demonstrated in literature due to challenges in the imaging scheme and the optimization in post-processing required at a wider field of view for sustaining high frame rates. These limit real-time visualization of complex urinary flow patterns (Nikolov & Jensen, 2001; Nikolov, 2002; Nikolov *et al.*, 2006). To address this issue and to improve the practicality of vector flow imaging of the LUT, a new flow imaging scheme making use of synthetic aperture imaging, and parallel computing techniques need to be devised to enable vector flow imaging at high frame rates in real-time (Jensen *et al.*, 2006).

2) ***Development of a real-time urethral resistance metric utilizing both PreWV and vector flow***

With local PreWV and urinary flow vectors along the urinary tract, a new real-time metric to locally estimate stiffness of the urethra can be realized. The relationship between flow and pressure can provide insight into the resistance of the conduit that is the urinary tract (Sekido, 2012; McDonough & Ryan, 2016). This metric can be used to differentiate between a healthy and BPH diseased subject for a comprehensive evaluation during patient voiding in real-time by utilizing the sub-ms temporal resolution that HiFRUS enables. An *in-vitro* evaluation needs to be done using the existing phantoms and programmable ultrasound system to calibrate the real-time performance of this metric prior to a case control study *in-vivo*. The resulting spatiotemporal resolution in quantifying the resistance along the urethra could be the calibrating factor in tuning this metric for real-time use. The anticipated outcome of this procedure would enable HiFRUS as a comprehensive tool to examine the morphological features of the male urinary tract system.

3) ***Verification and validation of this imaging framework through in-vivo study and analysis.***

To complete this proof-of-concept study, it is important to verify its performance *in-vivo*, and then validate the overall framework by comparing existing data from conventional urodynamic testing of BPH patients. The purpose of this study at the clinic would be to acquire data from male subjects with BPH, which can be regarded as the ‘case’ group, and to acquire data from a related group of subjects that could be identified as possibly developing BPH, which can be regarded as the ‘control’ group. Both raw data from this study need to be used to assess for factors of BPH using urethral resistance as a metric, which needs to be compared between the case and control groups to quantify the progression of BPH. The data collected also needs to be compared with available data from conventional urodynamic tests of BPH patients to validate the efficacy of such metrics for BPH progression. It is expected that this module may create

baseline data for the proposed new framework that urologists can use to evaluate the clinical value of the new metrics.

6.4 Research Summary

BPH is a noncancerous condition in aging males where an overgrowth of the prostate gland occurs. It notably leads to LUTS ranging from inconvenient nocturia to severe damage of the bladder from blockage, infection, and bladder stones. HiFRUS has enabled significant advances in urology through visualization of high temporal urinary flow dynamics within the male urinary tract during voiding. In this research, the utility of HiFRUS in this area has been extended by measuring the PreWV in an *in-vitro* urodynamic study for assessing the state of the urinary tract collapsed and bent state. A new tortuous flow phantom platform was devised to facilitate this *in-vitro* study to collect PreWV data using HiFRUS and perform tissue Doppler analysis. To study the effect in changing the tortuous geometry, the male urinary tract is modelled by two deformable bent geometry phantoms, one with 30° bend and another with 45° bend. These phantoms were fabricated using an adapted lost-core strategy protocol based in our lab. To study the effect in changing the collapsed state, the phantoms were deflated and encased in a tissue mimicking slab where the opening of the collapsed lumen was controlled in a flow circuit setup. Results from this experiment indicated good agreement with the ground truth measurements of the global PreWV, and the subregional and regional PreWV showed statistical significance that aligned well with existing theory in pressure wave propagation in human tissue. The outcome of this work supports further PreWV studies in analyzing the variables present in the BPH model of the male urethra using HiFRUS, and future research on novel non-invasive urodynamic studies for clinical translation.

REFERENCES

Abuhamad, A. (2014). Ultrasound in Obstetrics and Gynecology: A Practical Approach. *Chapter 1: Basic Physical Principles of Medical Ultrasound*, e-Book, First Edition.

Alastruey, J., Hunt, A. A. E., Weinberg, P. D. (2014). Novel wave intensity analysis of arterial pulse wave propagation accounting for peripheral reflections. *Int. j. numer. method. biomed. eng., 30*, 249–279.

Anderson, W. A. D. (1953). Pathology. Published by The C. V. Mosby Co, St. Louis, MO.

Angelsen, B. A. J., *et al.* (1995). Which transducer array is best? *Eur. J. Ultrasound, 2*(2), 151-164. doi: 10.1016/0929-8266(95)00092-5.

Arora, D., Cooley, D., Perry, T., Skliar, M., Roemer, R.B. (2005). Direct thermal dose control of constrained focused ultrasound treatments: Phantom and in vivo evaluation. *Phys Med Biol, 50*, 1919–1935.

Au, J. S., Hughson, R. L., Yu, A. C. H. (2018). Riding the plane wave: Considerations for in vivo study designs employing high frame rate ultrasound. *Appl. Sci.*, *8*, 286.

AUA Guideline. (2010). American Urological Association Guideline: Management of Benign Prostatic Hyperplasia (BPH). American Urological Association Education and Research, Inc.

AUA Guideline. (2019). Surgical Management of Lower Urinary Tract Symptoms Attributed to Benign Prostatic Hyperplasia: AUA GUIDELINE, American Urological Association (AUA).

Avdal, J., *et al*. (2017). Combined 2-D vector velocity imaging and tracking Doppler for improved vascular blood velocity quantification. *IEEE Transactions on Ultrasonics, Ferroelectrics, and Frequency Control, 64*(12), 1795-1804. doi: 10.1109/TUFFC.2017.2757600.

Avolio, A., Chen, S., Wang, R., Zhang, C., Li, M., O'Rourke, M. (1983). Effects of aging on changing arterial compliance and left ventricular load in a northern Chinese urban community. *Circulation, 68*, 50-58.

Badescu, E., Ambrogio, S., Fenner, J., Liebgott, H., Friboulet, D., Garcia, D. (2018). Vortex ring phantom for investigation of ultrasound vector flow. *IEEE International Ultrasonics symposium*, Kobe, Japan.

Baker, D. W. (1970). Pulsed ultrasonic Doppler blood-flow sensing. *IEEE Transactions on Sonics and Ultrasonics, 17*(3), 170-184. doi: 10.1109/T-SU.1970.29558.

Bakke, T. (1973). A new mechanical instrument for the measurement of fibro-elasticity, with special reference to its use in the assessment of the consistency of the uterine cervix. *Acta Obstet. Gynecol. Scand., 52*, 277-287.

Bergel, H. D. (1972). The properties of blood vessels. In: Fung Y, Perrone N, Anliker M (eds) *Biomechanics, its foundations and objectives*. Prentice Hall, New Jersey, 105-139.

Blake, C., Abrams, P. (2004). Non invasive techniques for the measurement of isovolumetric bladder pressure. *J Urol., 171*, 12-19.

Boice, E. N., Berard, D., Gonzalez, J. M., Hernandez Torres, S. I., Knowlton, Z. J., Avital, G., Snider, E. J. (2022). Development of a modular tissue phantom for evaluating vascular access devices. *Bioengineering, 9*, 319. Available: https://doi.org/10.3390/ bioengineering9070319.

Boni, E., Bassi, L., Dallai, A., *et al.* (2017). Architecture of an ultrasound system for continuous real-time high frame rate imaging. *IEEE Trans. Ultrason. Ferroelectr. Freq. Control, 64*, 1276–1284.

Borlotti, A., Khir, A. W., Rietzschel, E. R., *et al.* (2012). Noninvasive determination of local pulse wave velocity and wave intensity: Changes with age and gender in the carotid and femoral arteries of healthy human. *J Appl Physiol, vol. 113*, 727–735.

Bramwell, J. C., Hill, A. V. (1922). Velocity of transmission of the pulse wave and elasticity of arteries. *Lancet, 1*, 891.

Brands, P. J., Willigers, J. M., Ledoux, L. A. F., *et al.* (1998). A noninvasive method to estimate pulse wave velocity in arteries locally by means of ultrasound. *Ultrasound Med. Biol., 24*, 1325–1335.

Burckhardt, C. E., Grandchamp, P. -A., Hoffmann, H. (1974). An experimental 2 MHz synthetic aperture sonar system intended for medical use. *IEEE Transactions on Sonics and Ultrasonics, 21*(1), 1–6.

Calabia, J., Torguet, P., Garcia, M., *et al*. (2011). Doppler ultrasound in the measurement of pulse wave velocity: Agreement with the complior method. *Cardiovasc. Ultrasound, 9*.

Cao, R., Huang, Z., Varghese, T., Nabia, G. (2013). Tissue mimicking materials for the detection of prostate cancer using shear wave elastography: A validation study. *Med. Phys., 40*(2).

Chai, T. C. (2020). Personal communication from Toby C. Chai, MD, Chair, Department of Urology, Boston University School of Medicine, Chief of Urology, Boston Medical Center.

Chan, V., Perlas, A. (2011). Basics of Ultrasound Imaging. In *Atlas of Ultrasound-Guided Procedures in Interventional Pain Management*. New York, NY: Springer New York, pp. 13–19.

Chee, A. J., Ho, C. K., Yiu, B. Y., Yu, A. C. (2016). Walled carotid bifurcation phantoms for imaging investigations of vessel wall motion and blood flow dynamics. *IEEE Trans Ultrason Ferroelectr Freq Control, 63*,1852–1864.

Chen, H., Varghese, T., Rahko, P. S., Zagzebski, J. A. (2009). Ultrasound frame rate requirements for cardiac elastography: Experimental and in vivo results. *Ultrasonics, 49*, 98–111.

Choyke, P. L. (1995). Imaging of prostate cancer. *Abdominal Imaging, 20*, 505-515.

Corrado, P. A., Medero, R., Johnson, K. M., François, C. J., Roldán-Alzate, A., Wieben, O. (2021). A phantom study comparing radial trajectories for accelerated cardiac 4D flow MRI against a particle imaging velocimetry reference. *Magn Reson Med., 86*(1), 363–371.

David, R. H. J., Ashby, M. F. (2019). Engineering materials 1: An introduction to properties, applications and design. Fifth Edition, Butterworth-Heinemann, Elsevier.

De Korte, C. L., Fekkes, S., Nederveen, A. J., *et al.* (2016). Review: Mechanical characterization of carotid arteries and atherosclerotic plaques. *IEEE Trans. Ultrason. Ferroelectr. Freq. Control*, *63*, 1613–1623.

Dunmire, B., *et al*. (2000). Cross-beam vector Doppler ultrasound for angle-independent velocity measurements. *Ultrasound in Medicine and Biology, 26*(8), 1213-1235. Available: https://www.umbjournal.org/article/S0301-5629(00)00287-8/abstract. doi:10.1016/S0301-5629(00)00287-8.

Edwards, J. L. (2008). Diagnosis and management of benign prostatic hyperplasia. *Am. Fam. Physician, 77*(10), 1403-1410.

El-Zawahry, A., Alanee, S., Malan-Elzawahry, A. (2016). The use of urodynamics assessment before the surgical treatment of BPH. *Curr Urol Rep, 17*(10), 73. doi: 10.1007/s11934-016-0626-y.

Foster, H. E., *et al.* (2018). Surgical management of lower urinary tract symptoms attributed to benign prostatic hyperplasia: AUA Guideline. *Journal of Urology, 200*(3), 612-619. Available: https://www.auajournals.org/doi/10.1016/j.juro.2018.05.048. doi: 10.1016/j.juro.2018.05.048.

Fox, M. D. (1978). Multiple crossed-beam ultrasound Doppler velocimetry. *IEEE Transactions on Sonics and Ultrasonics, 25*(5), 281-286. doi: 10.1109/T-SU.1978.31028.

Fujikura, K., Luo, J., Gamarnik, V., *et al.* (2007). A novel noninvasive technique for pulse-wave imaging and characterization of clinically-significant vascular mechanical properties in vivo. *Ultrason. Imaging, 29*, 137–154.

Fung, Y. C. (1981). Biomechanics: mechanical properties of living tissues, Springer, NY.

Futterer, J. J., Heijmink, S. W., Spermon, J. R. (2008). Imaging the male reproductive tract: current trends and future directions. *Radiol Clin North Am., 46*, 133–47, vii. doi: 10.1016/j.rcl.2008.01.005.

Galosi, A. B., *et al*. (2012). Modifications of the bladder wall (organ damage) in patients with bladder outlet obstruction: ultrasound parameters. *Arch. Ital. Urol. Androl., 84*(4), 263-267.

Garra, B. S., Cespedes, E. I., Ophir, J., Spratt, S. R., Zuurbier, R. A., Magnant, C. M., Pennanen, M. F. (1997). Elastography of breast lesions: Initial clinical results. *Radiology, 202*, 79- 86.

Gennisson, J. L., Deffieux, T., Fink, M., Tanter, M. (2013). Ultrasound elastography: Principles and techniques. *Diagnostic and interventional imaging, 94*, 487-95.

Governatori, N., PollackJr., C. V. (2018). Hypertensive Crisis. *Cardiology Secrets*, Fifth Edition.

Griffiths, D. J. (1973). The mechanics of the urethra and of micturition. *Br J Urol., 45*, 497-507.

Hansen, J. M., Schaa, D., Jensen, J. A. (2011). Synthetic aperture beamformation using the GPU. *IEEE International Ultrasonics Symposium Proceedings*, 373-376. doi: 10.1109/ULTSYM.2011.0089.

Hansen, K. L., *et al.* (2016). Intra-operative vector flow imaging using ultrasound of the ascending aorta among 40 patients with normal, stenotic and replaced aortic valves. *Ultrasound in Medicine and Biology, 42*(10), 2414-2422. Available: https://www.umbjournal.org/article/S0301-5629(16)30140-5/abstract. doi: 10.1016/j.ultrasmedbio.2016.06.009.

Hansen, K. L., *et al*. (2017). Aortic valve stenosis increases helical flow and flow complexity: A study of intra-operative cardiac vector flow imaging. *Ultrasound in Medicine and Biology, 43*(8), 1607-1617. Available: https://www.umbjournal.org/article/S0301-5629(17)30140-0/abstract. doi: 10.1016/j.ultrasmedbio.2017.03.018.

Harley, R., James, D., Miller, A., White, J. W. (1977). Phonons and the elastic moduli of collagen and muscle. *Nature, 265*, 285-287.

Hirata, K., Yaginuma, T., O'Rourke, M. F., *et al.* (2006). Age-related changes in carotid artery flow and pressure pulses: Possible implications for cerebral microvascular disease. *Stroke, 37*, 2552–2556.

Ho, C. K., Chee, A. J. Y., Yiu, B. Y. S., Tsang, A. C. O., Chow, K. W., Yu, A. C. H. (2017). Wall-less flow phantoms with tortuous vascular geometries: design principles and a patient-specific model fabrication example. *IEEE Trans Ultrason Ferroelectr Freq Control, 64*, 25–38.

Humphrey, P. A. (2014). Male urethra and external genitalia anatomy. In: Brandes, S. B., Morey, A. F., eds. *Advanced Male Urethral and Genital Reconstructive Surgey. Current Clinical Urology*, New York, NY, Humana Press, 17–23.

Ishii, T., Kambara, Y., Yamanishi, T., Naya, Y., Igarashi, T. (2014a). Urine flow dynamics through prostatic urethra with tubular organ modeling using endoscopic imagery. *IEEE Journal of Translational Engineering in Health and Medicine, 2*, 1-9. doi: 10.1109/JTEHM.2014.2316148.

Ishii, T., Naya, Y., Yamanishi, T., Igarashi, T. (2014b). Urine flow dynamics through the urethra in patients with bladder outlet obstruction. *J Mech Med Biol., 14*, 1450052.

Ishii, T., Yiu, B. Y. S., Yu, A. C. H. (2017). Vector flow visualization of urinary flow dynamics in a bladder outlet obstruction model. *Ultrasound in Medicine and Biology, 43*(11), 2601-2610. Available: https://www.umbjournal.org/article/S0301-5629(17)30325-3/abstract. doi: 10.1016/j.ultrasmedbio.2017.07.006.

Ishii, T., Ho, C. K., Nahas, H., Yiu, B. Y. S., Chee, A. J. Y., Yu, A. C. H. (2019). Deformable phantoms of the prostatic urinary tract for urodynamic investigations. *Med Phys., 46*(7), 3034-3043.

Ishii, T., *et al.* (2020). Contrast-enhanced urodynamic vector projectile imaging (CE-UroVPI) for urethral voiding visualization: Principles and phantom studies. *Urology, 140*, 171-177. Available: https://www.goldjournal.net/article/S0090-4295(20)30271-5/abstract. doi: 10.1016/j.urology.2020.03.005.

Jensen, J. A. (1995). An analysis of pulsed wave ultrasound systems for blood velocity estimation. 22nd Edition.

Jensen, J. A., Munk, P. (1998). A new method for estimation of velocity vectors. *IEEE Transactions on Ultrasonics, Ferroelectrics, and Frequency Control, 45*(3), 837-851. doi: 10.1109/58.677749.

Jensen, J. A., *et al.* (2006). Synthetic aperture ultrasound imaging. *Ultrasonics, 44*, e5-e15. Available: http://www.sciencedirect.com/science/article/pii/S0041624X06003374. doi: 10.1016/j.ultras.2006.07.017.

Jensen, J. A. (2007). Medical ultrasound imaging. *Prog. Biophys. Mol. Biol., 93*, 153–165.

Jensen, J., *et al.* (2014). Accuracy and sources of error for an angle independent volume flow estimator. doi: 10.1109/ULTSYM.2014.0425.

Jensen, J. (2017). Fast plane wave imaging. Technical University of Denmark.

Johnson, S. A. *et al.* (1975). Digital computer simulation study of a real-time collection, Post-processing synthetic focusing ultrasound cardiac camera. *In Acoustical Holography. Boston*, MA: Springer US, 193–211.

Kasai, C., *et al.* (1985). Real-time two-dimensional blood flow imaging using an autocorrelation technique. *IEEE Transactions on Sonics and Ultrasonics*, *32*(3), 458-464. doi: 10.1109/T-SU.1985.31615.

Kharine, A., Manohar, S., Seeton, R., Kolkman, R. G. M., Bolt, R. A., Steenbergen, W., de Mul, F. F. M. (2003). Poly(vinyl alcohol) gels for use as tissue phantoms in photoacoustic mammography. *Phys Med Biol, 48*, 357-370.

Kortbek, J., Jensen, J. A. (2006). Estimation of velocity vector angles using the directional cross-correlation method. *IEEE Transactions on Ultrasonics, Ferroelectrics, and Frequency Control, 53*(11), 2036-2049. doi: 10.1109/TUFFC.2006.144.

Krokosky, E., Krouskop, T. (1968). A stress deformation model of the human aorta. *J. Biomed. Materials Res., 2*, 503-525.

Kroner, E. S. J., Lamb, H. J., Siebelink, H. -M. J., *et al.* (2014). Pulse wave velocity and flow in the carotid artery versus the aortic arch: Effects of aging. *J. Magn. Reson. Imaging*, *40*, 287–293.

Krouskop, T. A., Dougherty, D. R., Vinson, F. S. (1987). A pulsed Doppler ultrasonic system for making noninvasive measurements of the mechanical properties of soft tissue. *J. Rehabil. Res. Dev., 24*, 1–8.

Krouskop, T. A., Wheeler, T. M., Kallel, F., Garra, B. S., Hall, T. (1998). Elastic moduli of breast and prostate tissues under compression. *Ultrasonic Imaging, 20*, 260-274.

Kumar, Y. N., Singh, Z., Wang, Y. -N, Schade, G. R., Kreider, W., Bruce, M., Vlaisavljevich, E., Khokhlova, T. D., Maxwell, A. D. (2022). Development of tough hydrogel phantoms to mimic fibrous tissue for focused ultrasound therapies. *Ultrasound in Medicine & Biology, 48*(9), 1762-1777.

Lai, S. S. M., *et al.* (2013). Design of anthropomorphic flow phantoms based on rapid prototyping of compliant vessel geometries. *Ultrasound in Medicine and Biology, 39*(9), 1654-1664. Available: https://www.umbjournal.org/article/S0301-5629(13)00595-4/abstract. doi: 10.1016/j.ultrasmedbio.2013.03.015.

LCMC. (2012). Basic Physical Principles of Ultrasound. *8th National Laser and Cosmetic Medicine Conference (LCMC 2012)*, Queensland, Australia, http://www.dcconferences.com.au/lcmc2012/pdf/Phlebology_PrereadingFriday.pdf.

Lee, W., Roh, Y. (2017). Ultrasonic transducers for medical diagnostic imaging. *Biomed. Eng. Lett., 7*(2), 91-97. doi: 10.1007/s13534-017-0021-8.

Lerner, L. B., McVary, K. T., Barry, M. J., *et al.* (2021a). Management of lower urinary tract symptoms attributed to benign prostatic hyperplasia: AUA Guideline part I, initial work-up and medical management. *J Urol, 206*, 806.

Lerner, L. B., McVary, K. T., Barry, M. J., *et al.* (2021b). Management of lower urinary tract symptoms attributed to benign prostatic hyperplasia: AUA Guideline part II, surgical evaluation and treatment. *J Urol, 206*, 818.

Li, R. X., Luo, J., Balaram, S. K., *et al.* (2013). Pulse wave imaging in normal, hypertensive and aneurysmal human aortas in vivo: A feasibility study. *Phys. Med. Biol.*, *58*, 4549–4562.

Li, Y., Gu, H., Fok, H., *et al.* (2017). Forward and backward pressure waveform morphology in hypertension. *Hyper*tension, 69, 375–381.

Loupas, L., Powers, J. T., Gill, R. W. (1995). An axial velocity estimator for ultrasound blood flow imaging, based on a full evaluation of the Doppler equation by means of a two-dimensional autocorrelation approach. *IEEE Transactions on Ultrasonics, Ferroelectrics, and Frequency Control, 42*(4), 672-688. doi: 10.1109/58.393110.

Loizou, C., Pattichis, C., Hooge, J. (2018). Handbook of speckle filtering and tracking in cardiovascular ultrasound imaging and video.

Luo, J., Li, R. X., Konofagou, E. E. (2012). Pulse wave imaging of the human carotid artery: An in vivo feasibility study. *IEEE Trans. Ultrason. Ferroelectr. Freq. Control*, *59*, 174–181.

Marwick, T. H. (2003). Stress echocardiography. *Heart, 89*, 113–118.

Masuno, G., *et al.* (2014). Two-dimensional blood flow vectors obtained with bidirectional doppler ultrasound. doi: 10.1109/EMBC.2014.6944770.

Maxwell, A. D., Wang, T, -Y., Yuan, L., Duryea, A. P., Xu, Z., Cain, C. A. (2010). A tissue phantom for visualization and measurement of ultrasound-induced cavitation damage. *Ultrasound in Medicine & Biology, 36*(12), 2132-2143.

McConnell, J., Roehrborn, C., Bautista, O., *et al.* (2003). The long-term effect of doxazosin, finasteride, and combination therapy on the clinical progression of benign prostatic hyperplasia. *N Engl J Med, 349*, 2387.

McDonough, R. C., Ryan, S. T. (2016). Diagnosis and management of lower urinary tract dysfunction. *Surg. Clin. North Am., 96*(3), 441–452. doi: 10.1016/j.suc.2016.02.003.

McNeal, J. E. (1981). The zonal anatomy of the prostate. *Prostate, 2*, 35–49.

McRae, L. P., Bottaccini, M. R., Gleason, D. M. (1995). Non invasive quantitative method for measuring isovolumetric bladder pressure and urethral resistance in the male: I. experimental validation of the theory. *Neurourol Urodyn., 14*, 101-114.

McVary, K. T. (2006). BPH: Epidemiology and Comorbidities. *Am J Manag Care, 12*(5 Suppl), S122-8.

Mehdizadeh, J. L., Leach, G. E. (2009). Role of invasive urodynamic testing in benign prostatic hyperplasia and male lower urinary tract symptoms. *Urol. Clin. North Am., 36*(4), 431-441. doi: 10.1016/j.ucl.2009.07.002.

Mitterberger, M., *et al.* (2010). Ultrasound of the prostate. *Cancer Imaging, 10*(1), 40–48. doi: 10.1102/1470-7330.2010.0004.

Montaldo, G., Tanter, M., Bercoff, J., *et al.* (2009). Coherent plane-wave compounding for very high frame rate ultrasonography and transient elastography. *IEEE Trans. Ultrason. Ferroelectr. Freq. Control*, *56*, 489–506.

Moorthy, R. S. (2002). *Doppler ultrasound, 58*(1), 0–2. doi: 10.1016/s0377-1237(02)80001-6.

Mousavi, S. R., Sadeghi-Naini, A., Czarnota, G. J., Samani, A. (2014). Towards clinical prostate ultrasound elastography using full inversion approach. *Medical Physics, 41*, 033501. doi: 10.1118/1.4864476.

Munson, B. R., Young, D. F., Okiishi, T. H. (2006). Fundamentals of Fluid Mechanics, 5th Edition, Wiley.

Nabeel, P. M., Kiran, V. R., Joseph, J., *et al.* (2020). Local pulse wave velocity: Theory, methods, advancements, and clinical applications. *IEEE Reviews in Biomedical Engineering*, *13*. Institute of Electrical and Electronics Engineers, 74–112.

Natali, A. N., Carniel. E. L., Frigo, A., *et al.* (2016). Experimental investigation of the biomechanics of urethral tissues and structures. *Exp Physiol., 101*, 641–656.

Nguyen, T., *et al*. (2019). Pressure difference estimation in carotid bulbs using vector flow imaging - A phantom study. doi: 10.1109/ULTSYM.2019.8926268.

Nikolov, S. I., Jensen, J. A. (2001). Velocity estimation using synthetic aperture imaging [blood flow]. doi: 10.1109/ULTSYM.2001.991985.

Nikolov, S. I. (2002). Synthetic Aperture Tissue and Flow Ultrasound Imaging. *Ph.D. dissertation*, Dept. Elect. Eng, Tech. Univ. Denmark, Kongens Lyngby, Denmark.

Nikolov, S. I., Tomov, B. G., Jensen, J. A. (2006). Real-time synthetic aperture imaging: Opportunities and challenges. *Proc. Asilomar Conf. Signals Syst. Comp.*, 1548-1552. doi: 10.1109/ACSSC.2006.355018.

Nisar, H., Moore, J., Piazza, R., Maneas, E., Chen, E. C. S., Peters, T. M. (2020). A simple, realistic walled phantom for intravascular and intracardiac applications. *Int J Comput Assist Radiol Surg., 15*(9), 1513–1523.

Nitti, V. W. (2005). Pressure flow urodynamic studies: The gold standard for diagnosing bladder outlet obstruction. *Reviews in Urology, 7*(Suppl 6), S14-S21. Available: https://www.ncbi.nlm.nih.gov/pmc/articles/PMC1477621/.

O'Leary, M. (2000). LUTS, ED, QOL: alphabet soup or real concerns to aging men? *Urology, 56*, 7.

O'Rourke, M. F., Blazek, J. V., Morreels, C. L. Jr., Krovetz, L. J. (1968). Pressure wave transmission along the human aorta. Changes with age and in arterial degenerative disease. *Circ Res., 23*, 567–79.

Otto, C. M. (2012). The practice of clinical echocardiography, Elsevier/Saunders.

Parker, K. J., Huang, S. R., Musulin, R. A. (1990). Tissue response to mechanical vibrations for sonoelasticity imaging. *Ultras. Med. BioI., 16*, 241-246.

Pate, W. R., *et al.* (2020). Comparison of transabdominal and transrectal ultrasound for sizing of the prostate. *Urology, 141*, 125-129. Available: https://www.goldjournal.net/article/S0090-4295(20)30436-2/abstract. doi: 10.1016/j.urology.2020.04.054.

Pereira, T., Correia, C., Cardoso, J. (2015). Novel methods for pulse wave velocity measurement. *J. Med. Biol. Eng., 35*, 555–565.

Podkowa, A. S., Oelze, M. L., Ketterling, J. A. (2018). High-frame-rate Doppler ultrasound using a repeated transmit sequence. *Appl. Sci., 8*, 227. Available: http://dx.doi.org/10.3390/app8020227.

Pogue, B. W., Patterson, M. S. (2006). Review of tissue simulating phantoms for optical spectroscopy, imaging and dosimetry. *J Biomed Opt, 11*, Article 041102.

Rabben, S. I., Stergiopulos, N., Hellevik, L. R., *et al.* (2004). An ultrasound-based method for determining pulse wave velocity in superficial arteries. *J. Biomech., 37*, 1615–1622.

Rathaus, V., *et al*. (1991). Transperineal ultrasound examination in the evaluation of prostatic size. *Clin. Radiol., 44*(6), 383-385. doi: 10.1016/S0009-9260(05)80654-3.

Ricker, D. W. (2003). Chapter 1: Basic signal theory. *Echo Signal Processing*. Springer. ISBN 1-4020-7395-X.

Roehrborn, C. G., Girman, C. J., Rhodes, T., *et al.* (1997). Correlation between prostate size estimated by digital rectal examination and measured by transrectal ultrasound. *Urology., 49*, 548-557.

Salvi, P. (2017). Pulse waves: How vascular hemodynamics affects blood pressure. 2nd ed. Springer, Switzerland.

Sarvazyan, A. P. (1993). Shear acoustic properties of soft biological tissues in medical diagnostics. *J. Acoust. Soc. Am. Proc. 125th Meeting*, 2329.

Satomura, S. (1957). Ultrasonic Doppler method for the inspection of cardiac functions. *The Journal of the Acoustical Society of America, 29*(11), 1181-1185. Available: https://asa.scitation.org/doi/10.1121/1.1908737. doi: 10.1121/1.1908737.

Satomura, S. (1959). Study of the flow patterns in peripheral arteries by ultrasonics. *The Journal of the Acoustical Society of Japan*, *15*, 151-158.

Schafer, W. (1983). The contribution of the bladder outlet to the relation between pressure and flow rate during micturition. In: Hinman, F. Jr, Boyarsky, S., eds. *Benign Prostatic Hypertrophy*. New York, NY, Springer Verlag, 470-496.

Schafer, W. (1985). Urethral resistance? Urodynamic concepts of physiological and pathological bladder outlet function during voiding. *Neurourol Urodyn., 4*, 161-201.

Schafer, W., Kirschner-Hermans, R., Jakse, G. (1994). Non invasive pressure/flow measurement for precise grading of bladder outflow obstruction [abstract]. *J Urol., 151* (suppl.), 323A.

Sekido, N. (2012). Bladder contractility and urethral resistance relation: What does a pressure flow study tell us? *Int. J. Urology, 19*(3), 216–228. doi: 10.1111/j.1442-2042.2011.02947.x.

Sigel, B., Machi, J., Beitler, J., Justin, J. (1983). Red cell aggregation as a cause of blood-flow echogenicity. *Radiology, 148,*(3), 799-802. doi: 10.1148/radiology.148.3.6878705.

Sigrist, R. M. S., Liau, J., Kaffas, A. E., Chammas, M. C., Willmann, J. K. (2017). Ultrasound elastography: Riview of Techniques and clinical applications. *Theranostics, 7*(5), 1303-1329.

Tanter, M., Fink, M. (2014). Ultrafast imaging in biomedical ultrasound. *IEEE Transactions on Ultrasonics, Ferroelectrics, and Frequency Control, 61*(1), 102-119. doi: 10.1109/TUFFC.2014.2882.

Tarantini, S., Secomb, T. W., Hughes, A., *et al.* (2020). Measurement, analysis and interpretation of pressure/flow waves in blood vessels. *Front. Physiol, 11*, 1085, 2020.

Teixeira, R., Vieira, M. J., Gonçalves, A., *et al.* (2016). Ultrasonographic vascular mechanics to assess arterial stiffness: A review. *Eur. Heart J. Cardiovasc. Imaging*, *17*, 233–246.

Thorpe, A., Neal, D. (2003). Benign prostatic hyperplasia. *Lancet, 361*(9366), 1359-1367. doi: 10.1016/S0140-6736(03)13073-5.

Tojo, M., Yasuda, K., Yamanishi, T., Hattori, T., Nagashima, K., Shimazaki, J. (1994). Relationship between bladder neck diameter and hydraulic energy at maximum flow. *J Urol., 152*, 144–149.

Tortoli, P., Bambi, G., Ricci, S. (2006). Accurate Doppler angle estimation for vector flow measurements. *IEEE Transactions on Ultrasonics, Ferroelectrics, and Frequency Control, 53*(8), 1425-1431. doi: 10.1109/TUFFC.2006.1665099.

Vappou, J., Luo, J., Konofagou, E. E. (2010). Pulse wave imaging for noninvasive and quantitative measurement of arterial stiffness in vivo. *Am. J. Hypertens., 23*, 393–398.

Vos, T., *et al*. (2016). Global, regional, and national incidence, prevalence, and years lived with disability for 310 diseases and injuries, 1990–2015: a systematic analysis for the Global Burden of Disease Study 2015. *Lancet, 388*(10053), 1545-1602. doi: 10.1016/S0140-6736(16)31678-6.

Walz, M., Teubner, J., Georgi, M. (1993). Elasticity of benign and malignant breast lesions imaging, Application and results in clinical and general practice. *Eight Intern. Cong. Ultrasonic Exam. Breast.* 56.

Wan, Y., *et al.* (2013). Transrectal electrical impedance tomography of the prostate: spatially coregistered pathological findings for prostate cancer detection. *Med Phys, 40*(6), 063102. doi: 10.1118/1.4803498.

Wasserman, N. F. (2006). Benign prostatic hyperplasia: A review and ultrasound classification. *Radiologic Clinics of North America, 44*(5), 689-710.

Weerakkody, Y., Jones, J. (2022). Fetal heart rate in the first and second trimester. *Radiopaedia.org.* Available: https://doi.org/10.53347/rID-12798.

Wei, J. T., Calhoun, E., Jacobsen, S. J. (2005). Urologic diseases in America project: benign prostatic hyperplasia. *J. Urol., 173*(4), 1256-1261. doi: 10.1097/01.ju.0000155709.37840.fe.

Westerhof, N., Sipkema, P., Den Bos, G. C. V., *et al.* (1972). Forward and backward waves in the arterial system. *Cardiovasc. Res., 6*, 648–656.

Westerhof, N., Stergiopulos, N., Noble, M. I. M., *et al.* (2018). Snapshots of hemodynamics: An aid for clinical research and graduate education.

Yamada, H. (1970). Strength of biological materials. Williams & Wilkins Company, Baltimore, MD.

Yiu, B. Y. S., Tsang, I. K. H., Yu, A. C. H. (2011). GPU-based beamformer: Fast realization of plane wave compounding and synthetic aperture imaging. *IEEE Transactions on Ultrasonics, Ferroelectrics, and Frequency Control, 58*(8), 1698-1705. doi: 10.1109/TUFFC.2011.1999.

Yiu, B. Y. S., Yu, A. C. H. (2017). Spiral flow phantom for ultrasound flow imaging experimentation. *IEEE Transactions on Ultrasonics, Ferroelectrics, and Frequency Control, 64*(12), 1840-1848. doi: 10.1109/TUFFC.2017.2762860.

Zhang, M., Nigwekar, P., Castaneda, B., Hoyt, K., Joseph, J. V., Agnes, A., Messing, E. M., Strang, J. G., Rubens, D. J., Parker, K. J. (2008). Quantitative characterization of viscoelastic properties of human prostate correlated with histology. *J. Ultrasound Med. Biol., 34*(7), 1033–1042.

Zhang, S. -J., Qian, H. -N., Zhao, Y., Sun, K., Wang, H. -Q., Liang, G. -Q., Li, F. -H., Li, L. (2013). *Asian J Androl., 15*(1), 116–120.